FINAL REPORT

(NASA-CR-168842) A NEW NUMERICAL APPROACH FOR COMPRESSIBLE VISCOUS FLOWS Final Report (Georgia Inst. of Tech.) 105 p HC A06/MF A01 CSCL 20D
N82-22455
Unclas
G3/34 09714

A NEW NUMERICAL APPROACH FOR COMPRESSIBLE VISCOUS FLOWS

By

J. C. Wu

S. G. Lekoudis

Prepared for

NASA–Lewis Research Center

Under Grant No. NSG 3307

March 1982

GEORGIA INSTITUTE OF TECHNOLOGY

A UNIT OF THE UNIVERSITY SYSTEM OF GEORGIA

SCHOOL OF AEROSPACE ENGINEERING

ATLANTA, GEORGIA 30332

1982

Final Report

on NASA-Lewis Research Center
Grant No. NSG 3307

A NEW NUMERICAL APPROACH FOR COMPRESSIBLE VISCOUS FLOWS

by

J.C. Wu, Professor and
S.G. Lekoudis, Assistant Professor

School of Aerospace Engineering
Georgia Institute of Technology

TABLE OF CONTENTS

1. INTRODUCTION

The objective of the Grant NSG 3307, from the NASA Lewis Research Center to the School of Aerospace Engineering at Georgia Tech, was to develop a new numerical approach for computing unsteady compressible viscous flows. This approach offers the capability of confining the region of computation to the viscous region of the flow. The viscous region is defined as the region where the vorticity is nonnegligible and the difference in dilatation between the potential flow and the real flow around the same geometry is also nonnegligible. The method was developed and tested. Also, an application of the procedure to the solution of the steady Navier-Stokes equations for incompressible internal flows is presented.

2. MATHEMATICAL FORMULATION

In this chapter the mathematical relationships that govern the time history of compressible viscous flow around an arbitrary body are presented. The kinematic and kinetic boundary conditions are stated and a method for estimating the surface vorticity is described. In order to improve readability, the derivations of some of the equations used in this chapter are omitted in the main text and given in the appendices.

Governing Equations

In the absence of body forces, the Navier-Stokes equations for a compressible fluid with density ρ, viscosity ν, thermal conductivity k and ratio of specific heat coefficients γ, may be written in an inertial coordinate system as follows

$$\rho \frac{\partial \vec{V}}{\partial t} + \rho(\vec{V}.\vec{\nabla})\vec{V} = -\vec{\nabla}p + \vec{\nabla}.\vec{\vec{\tau}} \qquad (2.1)$$

The equation of continuity is given by

$$\frac{\partial \rho}{\partial t} + \vec{\nabla}.(\rho\vec{V}) = 0 \qquad (2.2)$$

The energy equation and the equation of state are given by

$$\rho \frac{\partial h}{\partial t} - \frac{\partial p}{\partial t} + \rho \, \vec{V}.(\vec{\nabla}h) - \vec{V}.\vec{\nabla}p = -\vec{\nabla}.q + \vec{\nabla}\vec{V}:\vec{\tau} \quad (2.3)$$

$$p = \rho RT = (\frac{\gamma-1}{\gamma})\rho h \quad (2.4)$$

Here $\vec{\nabla}\vec{V}:\vec{\tau}$ represents the dissipation function given in cartesian coordinates by

$$\vec{\nabla}\vec{V}:\vec{\tau} = \tau_{ij} \frac{\partial u_j}{\partial x_i}$$

where τ_{ij} is the shear stress tensor and can be expressed as follows;

$$\tau_{ij} = 2\mu \, e_{ij} + \delta_{ij} \, \lambda(\vec{\nabla}.\vec{V})$$

Here e_{ij} is the rate of strain tensor and λ is the second coefficient of viscosity.

Kinematics Expressed in Integral Representation

The vorticity $\vec{\omega}$ and the dilatation β are related to the velocity field $\vec{V}$ by:

$$\vec{\nabla} \times \vec{V} = \vec{\omega} \quad (2.5)$$

$$\vec{\nabla} \cdot \vec{V} = \beta \quad (2.6)$$

The kinematics of the problem, governed by equations (2.5) and (2.6) are elliptic in nature, requiring the specification of Neuman, Dirichlet or mixed type of boundary conditions for velocity. These conditions are required both at infinity, known as the farstream condition, and on the solid surface. In the present study, Dirichlet type boundary conditions are prescribed on the boundaries.

The velocity boundary conditions are

$$\vec{V} = \vec{V}_b \qquad \text{on } b \tag{2.7}$$

and R is the fluid domain bounded by the boundary b. For external flow problems, the boundary b consists of the farstream boundary c and the body surface s. On s, the no-slip condition is used, while $\vec{V} = \vec{V}_\infty$ is prescribed on c.

Since the kinematic relationships are linear in $\vec{V}$, the velocity vector $\vec{V}$ can be decomposed into a solenoidal part $\vec{V}_1$ and an irrotational part $\vec{V}_2$ with homogeneous boundary condition for the latter. Thus

$$\vec{V} = \vec{V}_1 + \vec{V}_2 \tag{2.8}$$

with

$$\vec{\nabla} \cdot \vec{V}_1 = 0 \tag{2.9a}$$

$$\vec{\nabla} \times \vec{V}_1 = \vec{\omega} \tag{2.9b}$$

having boundary conditions

$$\vec{V}_{1s} = 0 \tag{2.10a}$$

$$\vec{V}_{1c} = \vec{V}_\infty \tag{2.10b}$$

and, for $\vec{V}_2$,

$$\vec{\nabla} \cdot \vec{V}_2 = \beta \qquad (2.11a)$$

$$\vec{\nabla} \times \vec{V}_2 = 0 \qquad (2.11b)$$

with boundary conditions

$$\vec{V}_{2s} = 0 \qquad (2.12a)$$

$$\vec{V}_{2c} = 0 \qquad (2.12b)$$

Wu (1) has shown that it is possible to recast the kinematic aspect of the problem into an integral representation for the velocity $\vec{V}$ in terms of the vorticity $\vec{\omega}$ and the dilatation β. For two dimensional flows this means

$$\vec{V}(\vec{r}_o,t) = -\frac{1}{2\pi}\int_R \frac{\vec{\omega}\times(\vec{r}-\vec{r}_o) + \beta(\vec{r}-\vec{r}_o)}{|\vec{r}-\vec{r}_o|^2}\, dR + \vec{V}_\infty \qquad (2.13)$$

In (2.13) R is the region where the vorticity and dilatation are non-negligible. At high and moderate Reynolds number the dilatation is significant at distances from the body where the vorticity is already negligible. Hence the approach does not seem as advantageous as in the incompressible case. However, by using the potential flow solution around the same body, it will be shown in the next section that the domain of the computations can be reduced to include only the region where the vorticity and the difference in dilatation between the viscous flow and potential flow are both non-negligible.

<u>Use of the Potential Flow Solution to Reduce the Domain of Computations</u>

Equation (2.13) can be written in the following form

$$\vec{V}(\vec{r}_o,t) = -\frac{1}{2\pi}\int_{R1}\frac{\vec{\omega}\times(\vec{r}-\vec{r}_o)+\beta(\vec{r}-\vec{r}_o)}{|\vec{r}-\vec{r}_o|^2}\,dR$$

$$-\frac{1}{2}\int_{R2}\frac{\beta(\vec{r}-\vec{r}_o)}{|\vec{r}-\vec{r}_o|^2}+\vec{V}_\infty \qquad (2.14)$$

where R1 is the region of the flow where vorticity is non-negligible and R2 is the rest of the domain, extending to infinity for external flow problems. This expression can be written for the potential flow around the same body as follows:

$$\vec{V}_p(\vec{r}_o) = -\frac{1}{2\pi}\int_{R1}\frac{\beta_p(\vec{r}-\vec{r}_o)dR}{|\vec{r}-\vec{r}_o|^2}-\frac{1}{2\pi}\int_{R2}\frac{\beta_p(\vec{r}-\vec{r}_o)dR}{|\vec{r}-\vec{r}_o|^2}$$

$$-\frac{1}{2\pi}\int_{s}\frac{\gamma_p\times(\vec{r}-\vec{r}_o)dS}{|\vec{r}-\vec{r}_o|^2}+\vec{V}_\infty \qquad (2.15)$$

where the subscript p indicates potential flow and γ_p is the vortex sheet strength on the surface, s, of the body due to the potential flow. Because equation (2.15) is a limiting case of the general viscous compressible flow relation (2.14), it gives the potential velocity everywhere except at the surface where the equation is identically zero.

If region R1 extends far enough from the body, the combination of (2.14) and (2.15) gives

$$\vec{V}(\vec{r}_o,t) = -\frac{1}{2\pi}\int_{R1}\frac{\vec{\omega}\times(\vec{r}-\vec{r}_o)+(\beta-\beta_p)(\vec{r}-\vec{r}_o)}{|\vec{r}-\vec{r}_o|^2}\,dR$$

$$-\frac{1}{2\pi}\int_s\frac{\gamma_p\times(\vec{r}-\vec{r}_o)ds}{|\vec{r}-\vec{r}_o|^2}+\vec{V}_p \qquad (2.16)$$

The relation (2.16) implies the following. First, $(\beta-\beta_p)$ in region R2 is small enough so that its effect on the velocity in region R1 is negligible (a detailed discussion of this aspect is given in Reference 11). Second, one needs to solve only in region R1, which is a smaller region than the region where β is significant.

The kinematic boundary condition for the external flow problem requires that the velocity has to reach the freestream velocity at an infinite distance away from the solid surfaces. This requirement is referred to in this work as the farfield boundary conditions. This requirement is satisfied by equation (2.16). However, if a finite-difference method is used without any coordinate transformation, this boundary condition is difficult to satisfy since the computational domain to be included becomes very large.

Kinetics - The Vorticity, Dilatation, Density, and Energy Transport Equations

By taking the curl of equation (2.1) and using equation (2.4) one obtains

$$\frac{\partial \vec{\omega}}{\partial t} = \vec{\nabla} x \vec{V} x \vec{\omega} + (\frac{\gamma-1}{\gamma}) \vec{\nabla} \ln\rho \; x \vec{\nabla} h + \vec{\nabla} x \left\{ \frac{1}{\rho} \vec{\nabla} . \vec{\vec{\tau}} \right\} \tag{2.17}$$

Similarly, taking the divergence of equation (2.1) and using equation (2.4) results in

$$\frac{\partial \beta}{\partial t} = -\vec{\nabla}. \left[(\vec{V}.\vec{\nabla})\vec{V} \right] -(\frac{\gamma-1}{\gamma})\nabla^2 h \; -(\frac{\gamma-1}{\gamma})h\nabla^2 \ln\rho \; -(\frac{\gamma-1}{\gamma})\vec{\nabla}h.\vec{\nabla}\ln\rho$$

$$+ \vec{\nabla}.(\frac{1}{\rho} \vec{\nabla}.\vec{\vec{\tau}}) \tag{2.18}$$

Specializing the equations for two-dimensional case, rearranging the terms in equations (2.17) and (2.18), and collecting the coefficients of β and ω, equations (2.17) and (2.18) become

$$\frac{\partial \omega}{\partial t} = - \vec{\nabla}.(\vec{V}\omega) + (\frac{\mu}{Re.\rho})\nabla^2 \omega + \phi(\rho,\beta,\omega,h) \tag{2.19}$$

$$\frac{\partial \beta}{\partial t} = - \vec{\nabla}.(\vec{V}\beta) + (\frac{4\mu}{3.Re.\rho})\nabla^2 \beta + \chi(\rho,\beta,\omega, h) \tag{2.20}$$

The full details of the derivation of the above equations are given in appendix B.

The density and energy equations can be also written in terms of the derived variables ω and β as follows

$$\frac{\partial \ln\rho}{\partial t} = -\vec{\nabla}.(\vec{V}\ln\rho) - \Gamma \tag{2.21}$$

$$\frac{\partial h}{\partial t} = -\vec{\nabla}.(\vec{V}h) + (\frac{\gamma k}{Re.Pr.\rho})\nabla^2 h + \Theta(\rho,\beta,\omega, h) \tag{2.22}$$

where ω denotes the magnitude of the vorticity vector. The terms ϕ , χ , Γ and Θ look like source terms and are given in appendix B.

The governing equations (2.19) to (2.22) have been non-dimensionalized by normalizing the variables with respect to the following reference quantities: distance, L; velocity, V_∞; density, ρ_∞; enthalpy, V_∞^2 ; and time, L/V_∞, where L is the characteristic length of the body. This type of normalization leads to the following non-dimensional parameters: Mach number, M_∞; Reynolds number, Re; and Prandtl number, Pr.

Formulation for the Study of an Impulsively Started Airfoil

In this section, the mathematical formulation discussed above is specialized and applied to the study of compressible laminar flow past an impulsively started airfoil. The airfoil geometry and the grid system are generated through a conformal transformation which transforms the airfoil into a unit circle. The airfoil chosen for the numerical study is a modified 9% Joukowski airfoil.

By using the transformation relations given in appendix , the governing equations (2.19-2.22) are written in the transformed plane and in a conservation form as shown below.

The vorticity transport equation is

$$\frac{\partial\omega}{\partial t} = \frac{1}{H^2} \left(-\vec{\nabla}.(\vec{V}\omega)\right) + \frac{1}{H^2} \left(\frac{\mu}{\rho Re}\right) \nabla^2\omega + \frac{1}{H^2} \Phi \qquad (2.23)$$

where H is the scale factor.

The dilatation transport equation is

$$\frac{\partial\beta}{\partial t} = \frac{1}{H^2}\left(-\vec{\nabla}.(\vec{V}\beta)\right) + \frac{1}{H^2}\left(\frac{4.\mu}{3.Re.\rho}\right)\nabla^2\beta + \frac{1}{H^2}\chi \tag{2.24}$$

The density transport equation is

$$\frac{\partial \ln\rho}{\partial t} = \frac{1}{H^2}\left(-\vec{\nabla}.(\vec{V}\ln\rho)\right) - \Gamma \tag{2.25}$$

The energy transport equation is

$$\frac{\partial h}{\partial t} = \frac{1}{H^2}\left(-\vec{\nabla}.(\vec{V}h)\right) + \frac{1}{H^2}\left(\frac{\gamma k}{Re.Pr.\rho}\right)\nabla^2 h + \theta \tag{2.26}$$

where $\vec{V}$ is the apparent velocity in the transformed plane and the divergence and Laplacian operators are applied in the transformed plane. The source terms ϕ, χ, Γ and θ are given in appendix A.

The radial and tangential components of the velocity in the transformed plane are

$$\vec{V}_\theta(\vec{r}_o,t) = \frac{1}{2\pi}\int_s \frac{\gamma_p.H(r\cos(\theta-\theta_o)-r_o)ds}{|\vec{r}-\vec{r}_o|^2} + V_{\theta_p}$$

$$- \frac{1}{2\pi}\int_{R1} \frac{\omega H^2(r\ \cos(\theta-\theta_o)-r_o)dR}{|\vec{r}-\vec{r}_o|^2} - \frac{1}{2\pi}\int_{R1} \frac{H^2(\beta-\beta_p)r^2\sin(\theta-\theta_o)dR}{|\vec{r}-\vec{r}_o|^2} \tag{2.27}$$

$$V_r(\vec{r}_o,t) = -\frac{1}{2\pi}\int_s \frac{\gamma_p H.r\ \sin(\theta-\theta_o)ds}{|\vec{r}_s-\vec{r}_o|^2} + \frac{1}{2\pi}\int_{R1} \frac{\omega H^2 r\ \sin(\theta-\theta_p)dR}{|\vec{r}-\vec{r}_o|^2}$$

$$- \frac{1}{2\pi} \int_{R1} \frac{(\beta-\beta_p)(r \cos(\theta-\theta_o)-r_o)dR}{|\vec{r}-\vec{r}_o|^2} + V_{r_p} \qquad (2.28)$$

Equations (2.27) and (2.28) are essentially the same as the two components of equation (2.16) in cylinderical coordinates, except for the scale factor H.

Surface Vorticity Determination

The vorticity values away from the surface are determined using the vorticity transport equation (2.23). In order to solve this equation, it is necessary to prescribe the vorticity values on the solid surface at all time levels. To do that, the viscous region is conveniently divided into a vortex sheet of strength γ located on the surface, and an outer vorticity field where the vorticity ω and the dilatation β are assumed to be known. Applying equation (2.27) on the surface of the body yields

$$V_\theta(r_s,t) = 0 = - \frac{1}{2\pi} \int_s \frac{H(\gamma-\gamma_p)(r_s\cos(\theta-\theta_o)-r_s)d\theta}{r_s^2 + r_s^2 - 2r_s^2 \cos(\theta-\theta_o)} + V_t \qquad (2.29)$$

Here γ represents the integrated value of ωdn on the first cell adjacent to the surface and r_s is the position vector for the points on the surface where the tangential component is calculated. V_t is the tangential velocity at the body surface due to both the outer vorticity field and the whole dilatation field in R1, and is given by

$$V_t = -\frac{1}{2\pi}\int_{R1}\frac{\omega H^2(r\cos(\theta-\theta_o)-r_o)rdrd\theta}{r^2+r_o^2-2rr_o\cos(\theta-\theta_o)} - \frac{1}{2\pi}\int_{R1}\frac{(\beta-\beta_p)H^2 r\sin(\theta-\theta_o)rdrd\theta}{r^2+r_o^2-2rr_o\cos(\theta-\theta_o)} \tag{2.30}$$

It must be noted that the region R1 in the first integral does not include points on the solid surface.

If r approach r_s, the first integral on the right-hand side of equation (2.29) becomes [20].

$$-\frac{1}{2\pi}\int_s\frac{(\gamma-\gamma_p)H(r_s\cos(\theta-\theta_o)-r_s)rd\theta}{r_s^2+r_s^2-2r_s^2\cos(\theta-\theta_o)} = \frac{1}{4\pi}\int_0^{2\pi}(\gamma-\gamma_p)Hds - \frac{1}{2}(\gamma-\gamma_p)H \tag{2.31}$$

The principle of conservation of total vorticity gives

$$\frac{1}{4\pi}\int_0^{2\pi}\gamma H\, r_s\, d\theta = -\frac{1}{4\pi}\int_{(R1-s)} H^2\omega\, dR \tag{2.32}$$

and, since the solution is started by a non-circulatory potential flow, it follows that

$$\frac{1}{4\pi}\int_0^{2\pi}\gamma_p . H\, r_s\, d\theta = 0 \tag{2.33}$$

Substituting equations (2.30-2.33) into equation (2.29) yields

$$\gamma H = \frac{1}{2\pi r_s}\int_{(R1-s)}\frac{(r_s^2-r^2)\omega H^2\, rdrd\theta}{r_s^2+r^2-2rr_s\cos(\theta-\theta_o)} - \frac{1}{\pi}\int_{R1}\frac{H^2(\beta-\beta_p)r\sin(\theta-\theta_o)rdrd\theta}{r_s^2+r^2-2rr_s\cos(\theta-\theta_o)} + \gamma_p H \tag{2.34}$$

In equation (2.34) the region (R1-s) is the computation region R1 excluding the surface s. Since the radius of the circle in the transformed plane is taken to be unity, equation (2.34) is rewritten as

$$\gamma = \frac{1}{2\pi H}\int_{(R1-s)} \frac{\omega H^2(1-r^2)rdrd\theta}{1+r^2-2r\cos(\theta-\theta_o)} - \frac{1}{\pi H}\int_{R1} \frac{H^2(\beta-\beta_p)r\sin(\theta-\theta_o)rdrd\theta}{1+r^2-2r\cos(\theta-\theta_o)} + \gamma_p \qquad (2.35)$$

Segmentation of the Velocity Field

The advantage of using equation (2.27) to calculate exterior flow problems stems from its explicit nature. Thus, the integral formulation permits the determination of the velocity on the boundaries of rectangular regions without regard to the interior nodes. In several cases, since rapid finite-difference computational schemes are available for solving the Poisson's equation in regions with rectangular boundaries, a combination of equation (2.27) and such schemes can provide a faster way to compute velocities in exterior flow problems. For this reason, the computational domain is divided into compartments in which the kinematic computations are performed independently of each other. The choice of the scheme, to be applied in each compartment, depends upon the shape of the body surface and on the relative distance between the body surface and the compartment. For example, as will be shown later in the static stall case, the integral relation (2.27) is used in the whole wake and in inner regions adjacent to the airfoil surface in order to compute the velocities. The

Poisson's equation is used in the rest of the computational domain and the velocity on the boundaries is calculated using the integral relation (2.27).

The Poisson's equation for the tangential velocity in the transformed plane is derived as follows:

The vorticity and dilatation can be written as

$$\vec{\nabla} \times \vec{V} = \vec{\omega} H^2 = \vec{\omega}_o \tag{2.36}$$

$$\vec{\nabla} \cdot \vec{V} = \beta H^2 = \beta_o \tag{2.37}$$

Upon taking the curl of the terms in equation (2.36), the equation becomes

$$\vec{\nabla} \times \vec{\omega}_o = \vec{\nabla} \times \vec{\nabla} \times \vec{V} = \vec{\nabla}(\vec{\nabla} . \vec{V}) - \nabla^2 \vec{V} \tag{2.38}$$

Substituting equation (2.37) in equation (2.38) one obtains:

$$\nabla^2 \vec{V} = \vec{\nabla} \beta_o - \vec{\nabla} \times \vec{\omega}_o \tag{2.39}$$

Writing equation (2.39) in polar coordinates

$$\left\{\frac{1}{r}\frac{\partial \omega_o}{\partial \theta} - \frac{\partial \beta_o}{\partial r}\right\} \vec{e}_r - \left\{\frac{\partial \omega_o}{\partial r} + \frac{1}{r}\frac{\partial \beta_o}{\partial \theta}\right\} \vec{e}_\theta + \nabla^2 V_\theta \vec{e}_\theta + \nabla^2 V_r \vec{e}_r = 0 \tag{2.40}$$

By singling out the tangential component terms in equation (2.40) one gets

$$\nabla^2 V_\theta = \frac{1}{r}\frac{\partial \beta_o}{\partial \theta} + \frac{\partial \omega_o}{\partial r} \tag{2.41}$$

Equation (2.41) is the Poisson's equation for the tangential velocity written in the transformed plane.

Once the tangential component of the velocity, V_θ, is determined the radial component of the velocity is calculated explicitly by using the definition of the dilatation in the transformed plane, namely

$$\vec{\nabla} \cdot \vec{V} = \beta H^2 = \beta_o$$

$$\frac{\partial V_r}{\partial r} + \frac{V_r}{r} + \frac{1}{r}\frac{\partial V_\theta}{\partial \theta} = \beta_o \qquad (2.42)$$

Pressure and Shear Calculations

Since the surface pressure details are needed for any load estimation on the body surface, the equation of state (2.4) is used to determine the pressure on the surface as follows:

$$p = \left(\frac{\gamma-1}{\gamma}\right)\rho h \qquad (2.43)$$

A pressure coefficient can be written as

$$C_p = \frac{p-p_o}{(\frac{1}{2}\rho V_\infty^2)} \qquad (2.44)$$

where p_o is a reference pressure.

As will be shown later, the gradients of the flow variables on the upper surface of a stalled airfoil are very sensitive to small disturbances created either by using different approximations to the governing equations or by adopting different boundary conditions. Compressibility effects are expected to be small for $M_\infty = 0.4$, and in order to capture these small effects, it was decided to compare the present compressible results with incompressible results obtained by using exactly the same mathematical and numerical procedures. For this reason, a different (from that employed in the test cases) scheme for computing the surface pressure, similar to the scheme used in the incompressible case (7), is developed and presented below.

In the body-fitted coordinate system, the vector momentum equation is

$$\rho \frac{\partial \vec{V}}{\partial t} + \rho(\vec{V}.\vec{\nabla})\vec{V} = - \vec{\nabla}p + \vec{\nabla}. \vec{\vec{\tau}} \qquad (2.45)$$

At the surface, the momentum equation is reduced to the following simple form because of the no-slip condition.

$$\vec{\nabla}p = \vec{\nabla}. \vec{\vec{\tau}} \qquad (2.46)$$

Taking the dot product of the above equation with the tangential unit vector $\vec{t}$ at the surface, defined positive in the counterclockwise sense one gets

$$\frac{\partial p}{\partial s} = (\vec{\nabla}.\vec{\vec{\tau}}).\vec{t} \qquad (2.47)$$

where s is the coordinate direction tangential to the surface, and is measured positive in the counterclockwise sense.

The surface vector $\vec{t}$ is defined by

$$\vec{t} = \frac{dx}{ds}\,\vec{i} + \frac{dy}{ds}\,\vec{j} \tag{2.48}$$

For simplicity, it is assumed that the fluid is a perfect gas with constant molecular viscosity, thermal conductivity and specific heat. These assumptions are reasonable for low subsonic flows. By using these assumptions the right-hand side of equation (2.47) can be written as follows:

$$\vec{\nabla} \cdot \vec{\vec{\tau}} = \mu\nabla^2\vec{V} + 1/3\mu\vec{\nabla}\beta \tag{2.49}$$

Inserting equation (2.49) into equation (2.47) one gets

$$\frac{\partial p}{\partial s} = \mu\nabla^2 V_t + \left(\frac{1}{3}\right)\mu\,\frac{\partial \beta}{\partial s} \tag{2.50}$$

Also,

$$\nabla^2 V_t = \frac{\partial^2 V_t}{\partial s^2} + \frac{\partial^2 V_t}{\partial n^2} \tag{2.51}$$

where $\vec{n}$ is the unit normal vector on the body surface, measured positive in the direction away from the solid surface. Because of the no-slip condition, V_t and $\frac{\partial^2 V_t}{\partial s^2}$ are zero everywhere on the surface. Thus,

$$\nabla^2 V_t = \frac{\partial^2 V_t}{\partial n^2} = \frac{\partial \omega}{\partial n} \tag{2.52}$$

Combining the terms, equation (2.47) reduces to

$$\frac{\partial p}{\partial s} = \mu \frac{\partial \omega}{\partial n} + (1/3)\mu \frac{\partial \beta}{\partial s} \tag{2.53}$$

If the pressure is non-dimensionalized with respect to the dynamic pressure at infinity, and all quantities are non-dimensionalized with respect to the reference quantities mentioned earlier, equation (2.53) becomes

$$\frac{\partial C_p}{\partial s} = \frac{2C}{Re} \left(\frac{\partial \omega}{\partial n} + 1/3 \frac{\partial \beta}{\partial s}\right) \tag{2.54}$$

where, $C_p = \frac{p-p_o}{(\frac{1}{2}\rho V_\infty^2)}$ and C is the chord length.

The dimensionless shear stress at the surface is given by;

$$C_f = - \frac{2C}{Re} \omega \tag{2.55}$$

knowing the surface pressure and the surface shear stress distributions, other quantities of interest such as lift, drag and moment can be easily obtained.

Calculation of Loads

Once the surface pressure and shear stress distributions are known, the loads are obtained from the following expressions.

$$C_N = C_{N_p} + C_{N_F} \tag{2.56}$$

$$C_T = C_{T_p} + C_{T_F} \tag{2.57}$$

$$C_M = C_{M_p} + C_{M_F} \tag{2.58}$$

where

$$C_{N_p} = \frac{1}{C} \int_0^{2\pi} C_p(\theta) \frac{dx}{d\theta} d\theta \tag{2.59}$$

$$C_{N_F} = \frac{2}{Re} \int_0^{2\pi} \omega(\theta) \frac{dy}{d\theta} d\theta \tag{2.60}$$

$$C_{T_p} = -\frac{1}{C} \int_0^{2\pi} C_p(\theta) \frac{dy}{d\theta} d\theta \tag{2.61}$$

$$C_{T_F} = \frac{2}{Re} \int_0^{2\pi} \omega(\theta) \frac{dx}{d\theta} d\theta \tag{2.62}$$

$$C_{M_p} = \frac{1}{C^2} \int_0^{2\pi} C_p(\theta) \left\{ x\frac{dx}{d\theta} + y \frac{dy}{d\theta} \right\} d\theta \tag{2.63}$$

$$C_{M_F} = \frac{2}{Re.C} \int_0^{2\pi} \omega(\theta) \left\{ x \frac{dy}{d\theta} - y \frac{dx}{d\theta} \right\} d\theta \tag{2.64}$$

The C_N and C_T are force coefficients directed normal and tangential to the airfoil chord, and C_M is the moment coefficient. The subscripts p and f denote the pressure and the skin friction contribution respectively. The moment is taken about the origin ot the coordinate system and is positive in the counterclockwise direction.

The lift and drag coefficients referred to the wind axes are obtained from:

$$C_L = C_N \cos\alpha - C_T \sin\alpha \tag{2.65}$$

$$C_D = C_N \sin\alpha + C_T \cos\alpha \tag{2.66}$$

where α is the angle of attack.

Initial and Boundary Conditions

The non-circulatory potential flow solution is used as an initial condition in the present work. Along the body surface, the vanishing normal derivatives of enthalpy h and density ρ were used as boundary conditions for h and ρ. These conditions are convenient for an adiabatic wall. The surface values of the dilatation β were obtained using a three-point extrapolation formula during each iteration of the dilatation transport equation. The boundary values of β were relaxed and set to be zero whenever the solution approached steady state. The integral expression (2.35) was used to compute the surface vorticity at each iteration while iterating the vorticity transport equation.

The potential flow values were used as in flow boundary conditions, while the vanishing second derivatives for β, h,ρ and zero vorticity were used as downstream boundary conditions. The wake never approached the downstream boundary during the calculations. The aforementioned boundary conditions preserve the elliptic nature of the problem .

3. RESULTS AND DISCUSSION

The procedure developed was tested on two problems in order to demonstrate the ability of the approach to compute attached and separated flows. The test problems considered are: (i) laminar compressible flow around a circular cylinder, (ii) laminar compressible flow over an airfoil at zero angle of attack. Finally, the method was applied to the static stall problem.

In the results discussed below, the non-dimensionalization is done with respect to the free stream velocity and the characteristic length of the body in the transformed plane. In the airfoil case and other test cases, the solid body was set into motion impulsively. Since the time rate of change of all flow variables is very high after the impulsive start, very small values of the time step, Δt, are used to obtain proper timewise resolution at the initial time levels. As the gradients with respect to time decrease, large values of Δt are used. The under-relaxation parameter, which sometimes controls the acceleration of the convergence of the iterations, is varied depending upon the type of problem considered.

Laminar Compressible Flow Past a Circular Cylinder

The present scheme also has been applied to the study of laminar compressible flow past a circular cylinder at a Reynolds number of 40, Mach number of 0.4 and Prandtl number of 1. The Reynolds number is based on the cylinder diameter and the free stream velocity. This classical test case is chosen to demonstrate the ability of the approach to handle flows with massive separation.

The grid system consists of lines of constant radii and lines of constant angle θ. The lines of constant θ are equally spaced with $\pi/20$ intervals. In the radial direction, a stretching relation is assumed as follows:

$$r = e^s, \qquad s = (j-1)\Delta s, \; j = 1, Jmax$$

By varying s uniformly, with $\Delta s = 0.06$, an exponential variation is obtained. The total number of grid points used is 2000 points. It should be noted that with the present formulation not all of these grid points are involved in the computations at all time levels. At the earlier time levels, the computational region contained about 40% of the total number of grid points. As the solution progressed in time, the number of points in the computational domain increased. When the computations were terminated at a time level of 15.1, the computational region contained all the 2000 points.

In order to compute the kinematic part of the problem the segmentation technique, explained in chapter II was used. The computational domain is divided into three annular regions R', R" and R"'. The inner region, R', consists of 240 nodes. The intermediate region, R", consists of 600 nodes, while the outer region, R"', contains 1160 nodal points. Regions R', R" are matched at a distance of .35 radii away from the surface; likewise the regions R" and R"' are matched at a distance of 2.525 radii away from the surface. The far-field boundary is located 17.916 radii away from the surface. The integral formula is used to compute the tangential velocity in region R' and on all of the boundaries. Then, the Poisson's equation is iterated to get the velocities in R" and R"'.

The kinetic equations (2.19), (2.20), (2.21) and (2.22) are approximated by an implicit finite-difference scheme in the polar coordinates and are solved by using the 'point successive under-relaxation' technique. Central differences are used to approximate the convection terms. It should be noted that no symmetry was assumed regarding this present case.

The solid body was set into motion impulsively. At this impulsive start, the flow was prescribed by the potentialflow solution about a circular cylinder immersed in a uniform stream. The time step varied gradually from 0.05 to 0.15. The solution was terminated at $t = 15.1$. At this time level the drag coefficient had converged to three digits. In the present case, the time is non-dimensionalized relative to the cylinder radius and the free stream velocity.

In Figure 1 the surface pressure distribution at steady state is compared with the numerical solution obtained by Sankar and Tassa [2]. The agreement is quite good.

In Table 1, the present compressible and incompressible results are compared with the compressible results of Reference 2 . In this Table, the separation angle $\theta_{sep.}$ is measured from the rear axis, and obtained as the point on the surface where the vorticity changes sign. The length of the standing vortex (L/R) represents the distance between the center of the cylinder and the point on the centerline where the velocity changes sign. These comparisons indicate that the present solution and the finite-difference method give results that are in satisfactory agreement.

TABLE 1

Comparison Between the Present Method and Reference 2

	Presents Results		Reference 2
	Incompressible (M=0)	Compressible (M=0.4)	Compressible (M=0.4)
θ_{sep}	53.5	53.7	52.5
Length of Standing Vortex (L/R)	5.80	5.85	5.08
Pressure Drag Coefficient C_{D_P}	1.025	1.230	1.32
Friction Drag Coefficient C_{D_F}	0.555	.520	.561
Total Drag Coefficient C_{D_T}	1.580	1.750	1.881
Minimum Surface Vorticity $\omega_{min.}$	-6.60	-6.12	-5.82

Compressible Laminar Flow Past an Airfoil at Zero Angle of Attack

The computational procedure developed here is next applied to the case of compressible laminar flow past a symmetric 9% thick Joukowski airfoil at a zero angle of attack. The airfoil is obtained by means of a conformal transformation of a unit circle. **The chord Reynolds number** considered in this case is 1000. The Mach number is 0.4 and the Prandtl number is unity. The normalizing reference time is obtained by dividing the transformed circular cylinder radius by the free steam velocity. All of the quantities are non-dimensionalized with respect to the free stream velocity and cylinder radius.

The tangential velocity, V_θ , in the transformed plane, is calculated using the integral relation for the set of nodes on the first coordinate line next to the surface and at the outer boundaries. The Poisson's equation is then solved by using a 'successive point over-relaxation' technique in the rest of the domain. The difference kinetic equations, written in the transformed plane, are solved using a 'point under-relaxation' iterative technique. The circular domain is discretized with 60 equally spaced points in the direction and 40 points in the radial direction. The time step is gradually varied from 0.0025 to 0.1 during the course of the computations. The computations are initiated with an impulsive start. The initial surface vortex sheet strength is computed from the potential flow velocity values. The kinematic computations are done with the finite Fourier series method. At a time level of 6.5, a steady state is determined to have been reached based upon the agreement (within 1%) of the computed surface vorticity values with those of the previous time level.

In Figures 2, 3 the present surface pressure and surface vorticity values are compared with the corresponding values obtained in Reference 2 . Both solutions are in very close agreement. The reference pressure used in these figures is the free stream pressure.

Laminar Compressible Flow Past an Airfoil at an Angle of Attack

The airfoil used in the present study is the 9% thick symmetrical Joukowski airfoil described in appendix E. The chord Reynolds number considered is 1000. The Mach number is 0.4, the Prandtl number is 1.0 and the angle of attack is 15^{o}.

A number of publications (1, 2, 3, 5, 6, 7) have treated this problem before by incompressible flow. It can be seen from these results that the solutions are not quantitatively comparable. However, there is a qualitative similarity between the results. In the static stall case, the results depend on a number of factors such as grid resolution, specification of the far-field boundary conditions and the numerical scheme. Therefore, in order to capture the small compressibility effects expected here, the compressible results have been compared with incompressible results obtained using the same computer program after 'switching off' the compressibility effects.

Consequently, before solving the compressible static stall problem, it was appropriate to conduct first a series of incompressible numerical experiments to : (i) test the code, (ii) inspect the sensitivity of this solution with the change of mesh size in the θ direction, (iii) examine the role of the time increment on the accuracy of the solution, (iv) examine the cyclic behavior of the solution, and (v) obtain incompressible data to be compared later with the compressible data. The difference between the two solutions represents the effect of compressibility.

Incompressible Solution

The incompressible solution for the static stall case was obtained by following the same procedure used later for the compressible case. In order to demonstrate the accuracy of the scheme, the incompressible solution has been compared with the numerical results of Mehta [7]. As shown in Figure 4, the present results agree very well with Mehta's results at the early time levels. As expected, the two solutions differ quantitatively at the later time levels. However, the qualitative behavior is similar at these later time levels.

To illustrate the effect of the grid resolution on the solution, two sequences of solution were obtained for $\Delta\theta = \pi/24$ and $\Delta\theta = \pi/30$. Figure 5 shows the history of a load comparison between the two solutions. It is seen from this figure that the two solutions are comparable. Although there is no drastic difference between the two solutions, there still exists enough of a difference that there could be a misinterpretation of the results obtained for two different mesh size solutions, one compressible and the other incompressible. This experiment demonstrates the importance of using the same grid size whenever small compressibility effects are examined.

The continuation of the cyclic behavior of the solution for more than one cycle and the validity of the present method for a number of cycles of vortex shedding was demonstrated. The solution was advanced in time up to a dimensionless time level of 62 (the reference time being the transformed circle radius divided by the free-stream velocity). Figure 5 shows the time history of loads which illustrate the cyclic behavior of the solution with time. Note that there are two cycles observed in the prescribed time range. This exercise provides considerable confidence in the formulation of the problem and in the computer program.

Finally, in order to study the effect of the time step on the solution, three numerical experiments, with three different time increments, were performed. Table 2 shows the comparisons among these three solutions. Each solution has been started at time level of 20.175, and then advanced in time up to a time level of 21.615 and 24.735. The good agreement among the solutions is apparent in Table 2. It could be concluded that, within the prescribed time range, the size of the time step plays a minor role in the accuracy of the solution.

Table 2

Comparison Among Three Different Time Increments Solutions

Time Level	Δt	C_L	C_D	$-C_M$	$\omega_{s,min}$
	0.06	0.2582	0.1641	0.1160	-89.26
t = 21.615	0.12	0.2574	0.1654	0.1150	-89.41
	0.24	0.2623	0.1683	0.1127	-89.58
	0.06	0.3475	0.1722	0.1225	-93.971
t = 24.735	0.12	0.3516	0.1718	0.1235	-94.28
	0.24	0.3527	0.1686	0.1257	-94.46

Compressible Solution

In the Figures that follow, the chordwise distance denoted "chord percentage" is measured from the leading edge of the airfoil. The force coefficients are normalized with respect to the free-stream velocity and the radius of the unit circle. The normalized reference time is obtained by dividing the radius of the unit circle by the free-stream velocity.

The grid system contains 48 equally spaced points in the θ-direction and 40 points in the radial direction. The exponential relation given in appendix E is applied for placing the points in the r direction. The time increment used in this numerical study is progressively increased from Δt = 0.0005 to Δt = 0.24. A total of 255 time steps were used to march the solution to a time level of 31.275, when the computations were terminated.

Using the flowfield segmentation technique described earlier in chapter II, the velocity is obtained everywhere in the computational domain. Figure 6 shows the segmented compartments and the kinematic relation used in each of them.

The iterative procedure used in solving the kinetic equations were varied to study their effects on the solution. Switching the iteration direction in the tangential coordinates was used to accelerate the convergence. The convergence criteria used in solving the vorticity transport equation was based on the maximum vortex strength variations between two consecutive iterations, where the vortex sheet strength is defined by $\gamma = \omega H^2 dr$. Invariably, the maximum variation between two consecutive iterations occured near the trailing edge, which can be explained by examining equation (2.35). It is seen that the scale factor H appears in the denominator. Because the scale factor is very small near the trailing edge, it amplifies any error in the calculated value of the surface vortex sheet strength. The above criteria for convergence allows more tolerance for the vortex sheet strength near the trailing edge than anywhere else. The tolerance level specified for the vortex sheet strength was 0.002 at the earlier time levels and is subsequently reduced to 0.0005 at later time levels. Continuation of the iteration beyond the above tolerance limit was not found effective in reducing the residue. The residue instead oscillated around a minimum value without showing any tendency to reach zero.

The maximum tolerance criterion used in iterating the enthalpy and density transport equations are 0.1% and .5% of the previous iteration, respectively. In iterating for the dilatation transport equation, a stringent tolerance limit in the vicinity of the airfoil was assumed in order to ensure proper convergence. In the outer regions and near the trailing edge, this limit is relaxed to accelerate the convergence. At later time levels, the maximum allowable tolerance, in the inner regions, is taken to be 0.8%. This represents the maximum percentage variation between two consecutive iterations.

As described earlier, the total number of nodes are 1920. However not all of these nodes were involved in the computations at all time levels. At early time levels, the vortical region is confined to only about 25% of the maximum computational region. The computational time per time step depends on the extent of the computational boundary and varies from as little as 70 CPU seconds at the early time levels to 154 CPU seconds at later time levels on the CYBER-70 computer with a CDC 6400 CPU.

The average computational time required in the present study to advance the solution for one dimensionless time is 16 CPU minutes. Sankar and Tassa 2 used an ADI scheme to solve the primitive variable system of finite-difference equations, and took 11.5 CPU minutes to advance the solution for one dimensionless time on the same computer. It should be emphasized here that, in the present study, at later time levels the memory requirements are larger than those required in Reference 2. However, due to computer memory restrictions, the present computer program could not utilize the maximum capacity of the CYBER-70 computer. Therefore, unnecessary computations have been carried out for a number of time steps. Alternatively, if more computer core is used, along with using more sophisticated numerical procedures, it is believed that the computational time required to advance the solution for one dimensionless time can be reduced below 11.5 CPU minutes.

Table 3 gives the details of the time steps versus the computer time for the present computations.

Table 3

Sequence of Changing the Time Increment and

Summary of Computer Time

No. of Time Steps	Δt	Time Level T	Average CPU Time in Sec.*
10	0.0005	0.005	70
10	0.001	0.015	80
10	0.0015	0.03	85
10	0.0045	0.075	92
10	0.008	0.155	94
10	0.016	0.315	98
10	0.032	0.635	100
10	0.064	1.275	105
20	0.09	3.075	108
20	0.12	5.475	119
30	0.12	9.075	128
25	0.12	12.075	130
80	0.24	31.275	154

* CYBER-70/Model 74-6400 CPU.

Flow Development

The development of the flow field may be viewed as occuring in four stages. These are: (i) impulsive start, (ii) formation and growth of the primary bubble, (iii) the bursting of the primary bubble which is associated with the formation of both the secondary and the trailing edge bubbles, and (iv) reattachment of the primary bubble. The initial attached bubble which expands with time is referred as the 'primary bubble'.

The convention used is that the upper surface vorticity is negative for attached flows while positive vorticity indicates flow reversal. The opposite is true for the lower surface.

The first stage of the flow field development reflects the effects of the impulsive start. Immediately after the impulsive start, the vorticity is only non-zero at the surface, while potential flow exists in the rest of the fluid. The rear stagnation point is located on the upper surface of the airfoil. Within a short time, the rear stagnation point moves close to the trailing edge. This movement is associated with the formation of a "starting vortex". At subsequent time levels the boundary layer starts growing on the upper and lower surfaces of the airfoil. The thickness of the boundary layer on both the upper and lower surfaces increases with time, as is observed from the displacement of the 'streamline-like' lines near the surface. For convenience, the 'streamline like' lines will be called 'streamlines'. The thickness of the boundary layer on the lower surface is smaller than the thickness of the boundary layer on the upper surface due to the existence of a favorable pressure gradient on most of the lower surface. The extent of the region of adverse pressure gradient on the upper surface is shown in the pressure distribution plot. It is also observed, at this stage, that the magnitude of the surface vorticity near the leading edge on the upper surface continues to decrease with time, forecasting the onset of separation in that neighborhood when the surface vorticity changes sign. However, the separation does not actually occur until a time level of 1.88. During this first stage, and after the decay of the influence of the impulsive start, the value of C_L starts increasing due to the growth of circulation after first reaching a minimum value at T = 1.0 as shown in Figure 7. The value of C_D continually decreases because the decrease in the friction force on the lower surface as the positive vorticity decreases with time.

The second stage of flow development describes the occurrence of separation, together with the formation and growth of the primary bubble. The separation first takes place at 20% chord at T = 1.88. The size of the separation bubble increases with time until it covers most of the upper surface. This is expected, since the separation point moves forward towards the leading edge and the reattachment point moves rearward towards the trailing edge. At time level 7.214, the separation and the reattachment points are about 95% chord length apart. The increases in the size of the separation bubble increases the effective thickness of the airfoil, and the increase of the intensity of the reversed flow inside the bubble causes additional suction pressure on the upper surface. The above two factors result in an increase in the value of C_L with time. During the duration of the primary bubble, the drag coefficient remains approximately constant.

In the third stage of flow development, the primary bubble is ruptured and an open bubble is formed, indicating the cyclic start of vortex shedding. The reattachment point of the primary bubble lifts off at a time level of 7.214 causing separated flow over almost the entire upper surface. The increase in the number of streamline loops inside the separated bubble, indicates an intensification of the reversed flow inside the bubble. The flow rotation inside the bubble is clockwise, with the fluid next to the surface moving upstream. The pressure plots at T = 9.494, Figure 37, show a small region near the trailing edge where there is a decrease in the pressure in the direction of the main flow outside the bubble. This is equivalent to an adverse pressure gradient for the flow near the surface. A small counterclockwise separation bubble appears near the trailing edge at T = 11.775 as a result of the above mentioned pressure gradient. The size of this bubble increases slowly with time until it can be clearly seen at T = 14.05%. At this time level, a similar adverse pressure gradient develops at about 58% chordwise distance from the trailing edge. This results in the appearance of a secondary counterclockwise bubble at T = 16.71. The direction of the flow inside this bubble is counterclockwise, with the fluid near the surface moving downstream toward the trailing edge. The intensity of the flow rotation in the trailing edge bubble is larger than it is inside the secondary bubble, as indicated by the number of streamline loops inside that bubble. The size of the two bubbles increases with time. As time progresses, the primary bubble starts to shrink while the other two small bubbles enlarge. The secondary bubble expands locally in the normal direction, whereas the trailing edge bubble gets enlongated in the downstream direction. At this stage of flow development, the lift coefficient keeps on increasing, due to the extent of the primary bubble beyond the trailing edge, until it reaches a maximum at T = 10.75. Meanwhile, the drag coefficient starts increasing very slowly after the time level 4.8. This slow increase in the drag is due to the increase in the effective thickness of the airfoil as judged by the shape of the zero streamline. This causes an increase in the pressure drag. The value of C_D continuously increases until it reaches a maximum at T = 12. The downstream motion of the center of the ruptured clockwise bubble, which is accompanied by the appearance of the two small counterclockwise bubbles, causes a general drop in the value of C_L after T = 10.75. The reason for this drop is that the negative pressure sustained by the primary bubble is partly removed by the formation of the two counterclockwise bubbles. This also results in a decrease in the pressure drag, which explains the drop of C_D after reaching a maximum at T = 12.

The fourth stage of flow development involve the opening up of the secondary bubble, the lifting off of the trailing edge bubble, and the reattachment of the upstream part of the primary bubble. The streamlines and equi-vorticity lines show the following flow development during this stage: (1) the secondary bubble splits the primary bubble and opens up to the outside flow at a time level of 20.51; (2) the trailing edge bubble moves downstream until it lifts off the airfoil by T = 21.95; (3) the downstream part of the primary bubble starts to disengage from the surface at a time level of 25.455; and (4) as time progresses, the upstream part of the primary bubble spreads in the downstream direction until the reattachment point reaches the trailing edge at a time level of 31.275, indicating the completion of the first cycle of vortex shedding. The streamline pattern at T = 31.275 looks similar to the pattern at the start of the cycle (T = 7.214), which indicates that the second cycle of oscillatory behavior is going to start at T = 31.275. As the secondary bubble opens up to the main stream, the reattachment point of the upstream part of the primary bubble starts to move downstream, increasing the region of the clockwise reversed flow. This reversed flow is able to sustain more suction pressure which results in an increase in the value of C_L. The lift-off of the trailing edge bubble and the shedding of the downstream part of the primary bubble into the downstream flow enables the upstream part of the primary bubble to cover most of the airfoil. This will lead to a continuous increase in C_L and C_D, as indicated in Figures 8 and 9.

Judging either from the contour plots of the streamlines or from the time histories of the loads plots, it is estimated that one cycle of vortex shedding occurs during the time period from T = 7.214 to T = 31.275. With the airfoil chord as the characteristic length, the Strouhal number, defined by C/(TV), where T is the period of the cycle, is then found to be 0.155.

Comparison Between the Compressible and Incompressible Solutions

In order to predict the compressibility effect for the present static stall case at a Mach number of 0.4, the compressible and the incompressible solutions obtained using the same grid are quantitatively compared in Table 4. The importance of using the same grid size in both solutions was demonstrated earlier in this chapter.

Based on the comparison shown in Table 4, the observations made may be summarized as follows:

(i) At the earlier time levels, the compressibility seems to decrease the rate of thickening of the boundary layer.

(ii) The onset of the separation of the primary bubble begins to appear at a later time level in the compressible case.

(iii) Compressibility seems to play a minor role in the growth of the primary bubble.

(iv) The compressibility delays the appearance of both the secondary and the trailing edge bubbles. These two bubbles grow at a faster rate in the compressible case than they grow in the incompressible case as shown in Figures (8-10).

(v) When the first cycle of vortex shedding starts, the difference in the force coefficients between the compressible and the incompressible solutions is small. As time advances, the difference between the two solutions gradually increases, indicating the increased influence of the compressibility. At a time level of approximately 21 the compressibility effect becomes very small. At this time level, the time rate of change of flow variables decreases to a minimum. At later time levels, $T = 23 - 31.275$, the compressibility effect appears to increase again but at a slower rate.

(vi) The effect of compressibility on the force coefficients is shown in Figures (8-10). This effect is comparable to the one computed in Reference 2, as shown in Figures 11 and 12.

Table 4,

Quantitative Comparison Between the Present Incompressible and Compressible Solutions

Flow Events	Compressible Data	Incompressible Data
Onset of separation of the primary bubble	T = 1.88	T = 1.76
Separation location from leading edge	20%	23%
Cycle begins at T =	7.214	6.821
Cycle ends at T =	31.275	29.815
First appearance of trailing edge bubble	T = 11.775	T = 11.24
First appearance of secondary bubble	T = 16.70	T = 15.374
Opening up of the secondary bubble	T = 20.51	T = 19.81
Strouhal number $C/(TV_\infty)$	0.15478	0.16146
$C_{L_{max.}}$	1.32	1.29
$C_{L_{min.}}$	0.254	0.262

* The force coefficients are given after the recovery from the impulsive start.

Comparison With Other Numerical Solutions

The flow around a 9% symmetric Joukowski airfoil at an angle of attack of 15°, chord Reynolds number of 1000, Mach number of 0.4 and Prandtl number of one, has been solved numerically by Sankar and Tassa [2].

The computational procedures of Reference 2 are significantly different from those used in the present study, and it is very important to bear this in mind when comparing the results of the two studies. The procedures of Reference 2 are as follows: (1) the primative variables (u,V,ρ,h) are used as the unknown flow variables; (2) the governing equations are discretized using central difference formulas for the spatial derivatives; (3) a second order artificial diffusion is added to the real diffusion term to stabilize the solution; (4) an ADI procedure is used to solve the system of difference equations generated from the governing equations; (5) a fourth order dissipation term is added to the governing equations to eliminate the wiggles arising in the solutions; (6) the outer boundary is located at six chord lengths away from the airfoil (in the present study the outer bounday is located at about 10 chord lengths away from the surface); and (7) a uniform flow is used to start the solution impulsively.

Table 6 show typical comparison between the present results and the results obtained in Reference 15.

The stability requirement for non-linear problems may impose more restrictions on the size of the time step even in the case of implicit schemes [8] However, Desideri et al [9] and Ballhaus et al. [10], in separate studies, have shown that a cyclic variation of the size of the time step between two limits is helpful in obtaining convergence in the (ADI) schemes. In the present solution, no such restriction on the time step was required. It is believed that the use of the under-relaxation technique in solving the difference equations has a stabilizing effect on the solution. The maximum time step used in Reference 2 is 0.064, whereas, in the present study, the time size was successfully increased up to 0.24. More details about the work can be found in Reference 11.

Table 5

Quantitative Comparison Between the Present Results and Those of Reference 2

Flow Feature	Present Results	Reference 2
Onset of separation of the primary bubble	T = 1.88	T = 2.1719
Separation location from leading edge	20%	24%
Cycle begins at T =	7.214	6.3117
Cycle ends at T =	31.275	27.376
First appearance of the trailing edge bubble	T = 11.775	T = 10.695
First appearance of the secondary bubble	T = 16.70	T = 12.52
Opening up of the secondary bubble	T = 20.51	T = 18.056
Strouhal number $C/(TV_{\infty})$	0.15478	0.17626
$C_{L\ max.}$	1.32	1.34
$C_{L\ min.}$	0.254	0.251
$C_{D\ max.}$	0.346	0.364
$C_{D\ min.}$	0.165	0.141

4. THE USE OF THE INTEGRAL REPRESENTATION METHOD WITH SERIES SOLUTIONS FOR SOLVING THE NAVIER-STOKES EQUATIONS

The use of orthogonal functions in solving the Navier-Stokes equations has offered high accuracy for certain problems. The reason is the rapid decrease of the truncation error as the number of these functions used increase in a series representation of the solution (16). In this section of the report, the use of Fourier series with the integral representation method (1) is developed. The procedure is applied to simple test problems.

The Navier-Stokes equations, for steady incompressible flow, in a region R, with boundary B, can be written as follows (1):

$$\vec{v}(\vec{r}) = -\frac{1}{2\pi}\int_R \frac{\vec{\omega}_o \times (\vec{r}_o - \vec{r})}{|\vec{r}_o - \vec{r}|^2}\, dR_o + \frac{1}{2\pi}\int_B \frac{(\vec{v}_o \cdot \vec{n}_o)(\vec{r}_o - \vec{r})}{|\vec{r}_o - \vec{r}|^2}\, dB_o - \frac{1}{2\pi}\int_B \frac{(\vec{v}_o \times \vec{n}_o)\times(\vec{r}_o - \vec{r})}{|\vec{r}_o - \vec{r}|^2}\, dB_o \tag{4.1}$$

$$\vec{\omega} = -\frac{Re}{2\pi}\int_R \frac{(\vec{v}_o \times \vec{\omega}_o)\times(\vec{r}_o - \vec{r})}{|\vec{r}_o - \vec{r}|^2}\, dR_o + \frac{Re}{2\pi}\int_B \frac{h_o\, \vec{n}_o \times (\vec{r}_o - \vec{r})}{|\vec{r}_o - \vec{r}|^2}\, dB_o - \frac{1}{2\pi}\oint_B \frac{(\vec{\omega}_o \times \vec{n}_o)\times(\vec{r}_o - \vec{r})}{|\vec{r}_o - \vec{r}|^2}\, dB_o \tag{4.2}$$

Where $\vec{v}$ and $\vec{\omega}$ are the velocity and the vorticity vector respectively, $\vec{r}$ is the position vector and $\vec{n}$ is the unit vector on B directed outwards. The subscript o indicates that a variable or an integration is evaluated in the $\vec{r}_o$ space. Notice that (4.2) is nonlinear because it is equivalent to our familiar vorticity transport equation.

In a polar (r, θ) coordinate system, the vector equations (4.1) and (4.2) give the following scalar equations.

$$v_r = \frac{1}{2\pi} \int_R \frac{\omega_o r_o \sin(\theta_o - \theta)}{r_o^2 + r^2 - 2r_o r \cos(\theta_o - \theta)}$$

$$+ \frac{1}{2\pi} \oint_B \frac{v_{r_o}\left[r_o \cos(\theta_o - \theta) - r\right]}{r_o^2 + r^2 - 2r_o r \cos(\theta_o - \theta)} dB_o$$

$$- \frac{1}{2\pi} \oint_B \frac{v_{\theta_o} r_o \sin(\theta_o - \theta)}{r_o^2 + r^2 - 2r_o r \cos(\theta_o - \theta)} dB_o \tag{4.3}$$

$$v_\theta = - \frac{1}{2\pi} \int_R \frac{\omega_o r_o \cos(\theta_o - \theta) - r}{r_o^2 + r^2 - 2r_o r \cos(\theta_o - \theta)} dR_o$$

$$+ \frac{1}{2\pi} \oint_B \frac{v_{r_o} r_o \sin(\theta_o - \theta)}{r_o^2 + r^2 - 2r_o r \cos(\theta_o - \theta)} dB_o$$

$$+ \frac{1}{2\pi} \oint_B \frac{v_{\theta_o}\left[r_o \cos(\theta_o - \theta) - r\right]}{r_o^2 + r^2 - 2r_o r \cos(\theta_o - \theta)} dB_o \tag{4.4}$$

$$\omega = - \frac{Re}{2\pi} \int_R \frac{v_{r_o} \omega_o \left[r_o - r \cos(\theta_o - \theta)\right] + v_{\theta_o} \omega_o r \sin(\theta - \theta_o)}{r_o^2 + r^2 - 2r_o r \cos(\theta_o - \theta)} dR_o$$

$$+ \frac{Re}{2\pi} \oint_B \frac{h_o r \sin(\theta_o - \theta)}{r_o^2 + r^2 - 2r_o r \cos(\theta_o - \theta)} dB_o$$

$$+ \frac{1}{2\pi} \oint_B \frac{\omega_o \left[r_o - r \cos(\theta_o - \theta) \right]}{r_o^2 + r^2 - 2r_o r \cos(\theta_o - \theta)} dB_o \tag{4.5}$$

In (4.3) - (4.5) v_r and v_o denote the velocity components in the r and θ direction respectively. Because we are looking at a periodic in the θ-direction flowfield we can assume a solution in the form of finite Fourier series.

$$v_r = s_o + \sum_{n=1}^{N} (s_n \cos n\theta + t_n \sin n\theta) \tag{4.6}$$

$$v_\theta = p_o + \sum_{n=1}^{N} (p_n \cos n\theta + q_n \sin n\theta) \tag{4.7}$$

$$\omega = \alpha_o + \sum_{n=1}^{N} (\alpha_n \cos n\theta + \beta_n \sin n\theta) \tag{4.8}$$

In these equations, the Fourier coefficients α_o, α_n's, β_n's, s_o, s_n's, t_n's, p_o, p_n's, q_n's are dependent on r only.

Using the method of residuals (Appendix C), the integrals in equations (4.3), (4.4) and (4.5) could be evaluated explicitly and only the Fourier coefficients are left to be determined (Appendix C):

$$s_o = 0 \tag{4.9}$$

$$s_n = \frac{1}{2} \int_0^r \beta_n \left(\frac{r_o}{r}\right)^{n+1} dr_o + \frac{1}{2} \int_r^1 \beta_n \left(\frac{r}{r_o}\right)^{n-1} dr_o$$

$$+ \frac{1}{2} s_n(1)\, r^{n-1} - \frac{1}{2} q_n(1)\, r^{n-1} \tag{4.10}$$

$$t_n = -\frac{1}{2}\int_0^r \alpha_n\left(\frac{r_o}{r}\right)^{n+1} dr_o - \frac{1}{2}\int_r^1 \alpha_n\left(\frac{r}{r_o}\right)^{n-1} dr_o$$

$$+\frac{1}{2}\, t_n(1)\, r^{n-1} + \frac{1}{2}\, p_n(1)\, r^{n-1} \tag{4.11}$$

$$p_o = \int_0^r \alpha_o\left(\frac{r_o}{r}\right) dr_o \tag{4.12}$$

$$p_n = \frac{1}{2}\int_0^r \alpha_n\left(\frac{r_o}{r}\right)^{n+1} dr_o - \frac{1}{2}\int_r^1 \alpha_n\left(\frac{r}{r_o}\right)^{n-1} dr_o$$

$$+\frac{1}{2}\, t_n(1)\, r^{n-1} + \frac{1}{2}\, p_n(1)\, r^{n-1} \tag{4.13}$$

$$q_n = \frac{1}{2}\int_0^r \beta_n\left(\frac{r_o}{r}\right)^{n+1} dr_o - \frac{1}{2}\int_r^1 \beta_n\left(\frac{r}{r_o}\right)^{n-1} dr_o$$

$$-\frac{1}{2}\, s_n(1)\, r^{n-1} + \frac{1}{2}\, q_n(1)\, r^{n-1} \tag{4.14}$$

$$\alpha_o = \alpha_o(1) - Re\int_r^1 \xi_o\, dr_o \tag{4.15}$$

$$\alpha_n = \alpha_n(1)\, r^n - \frac{Re}{2}\, r^n \int_0^1 (\xi_n - \zeta_n)\, r_o^n\, dr_o$$

$$+\frac{Re}{2}\int_0^r (\xi_n - \zeta_n)\left(\frac{r_o}{r}\right)^n dr_o$$

$$-\frac{Re}{2}\int_r^1 (\xi_n + \zeta_n)\left(\frac{r}{r_o}\right)^n dr_o \tag{4.16}$$

$$\beta_n = \beta_n(1)\, r^n - \frac{Re}{2}\, r^n \int_0^1 (\eta_n + \mu_n)\, r_o^n\, dr_o$$

$$+\frac{Re}{2}\int_0^r (\eta_n + \mu_n)\left(\frac{r_o}{r}\right)^n dr_o$$

$$+ \frac{Re}{2} \int_r^1 (\eta_n - \mu_n)(\frac{r}{r_o})^n \, dr_o \qquad (4.17)$$

where $1 \leq n \leq N$, the quantities $s_n(1)$, $t_n(1)$, $p_n(1)$, $q_n(1)$ are the known velocity Fourier coefficients on boundary (or at r=1) and ξ, ζ, η, μ are the coefficients from convective terms:

$$\omega \, v_r = \xi_o + \sum_{n=1}^{N} (\xi_n \cos n\theta + \eta_n \sin n\theta) \qquad (4.18)$$

$$\omega \, v = \mu_o + \sum_{n=1}^{N} (\mu_n \cos n\theta + \zeta_n \sin n\theta) \qquad (4.19)$$

Once the Fourier coefficients of the velocities and the vorticity are determined, the velocity field and the vorticity field are easily calculated using equations (4.3) - (4.5).

Equations (4.9)-(4.17) are solved using an iterative procedure for the problem of steady flow inside a circle. The Fourier coefficients of the boundary velocities are assumed to be known.

Starting with known values of the Fourier coefficients of the vorticity , α_o^i, α_n^i's, β_n^i's, the superscript "i" being the iteration counter, the following steps constitute one iteration loop.

(i) Determine the boundary values $\alpha_o^i(1)$, $\alpha_n^i(1)$'s and $\beta_n^i(1)$'s.

The boundary values of the velocities need to be satisfied by equations (4.9)-(4.14) during each iteration. Thus with one set of α_o^i, α_n^i's and β_n^i's in R, the boundary values of $\alpha_o^i(1)$, $\alpha_n^i(1)$'s and $\beta_n^i(1)$'s are determined by

$$\int_o^1 \alpha_o r_o \, dr_o = p_o(1) \qquad (4.20)$$

$$\int_o^1 \alpha_n \, r_o^{\,n+1} \, dr_o = p_n(1) - t_n(1) \qquad (4.21)$$

$$\int_o^1 \beta_n \, r_o^{\,n+1} \, dr_o = s_n(1) + q_n(1) \qquad (4.22)$$

The equations (4.20)-(4.22) are the constrains on the boundary vorticity values derived from equations (4.9)-(4.14) when r=1. The $p_o(1)$, $p_n(1)$'s, $q_n(1)$'s, $s_n(1)$'s, $t_n(1)$'s are the Fourier coefficients of the velocities on the boundary which are assumed to be known. With the proper numerical integration of the integrals in equations (4.20)-(4.22), the values of α_o^i, α_n^i's and β_n^i's at r=1 are easily determined.

(ii) Compute the Fourier coefficients of the velocities in R.

With the proper numerical integration, equations (4.9)-(4.14) give explicit, point by point, calculation of s_n^i's, t_n^i's, p_o^2, p_n^i's, q_n^i's in the flow region R.

(iii) Compute the Fourier coefficients of the convective terms.

Because the Fourier coefficients of the velocities and of the vorticity are known at this stage, the Fourier coefficients ξ_o^i, ξ_n^i's, η_n^i's, μ_n^i's, ζ_n^i's can be determined using equations (4.18) and (4.19). The coefficient μ_o need not to be determined because it will not get into the calculation of the Fourier coefficients of the vorticity. This quantity is associated with the static pressure level and it remains arbitrary when the flow is incompressible.

(iv) Compute the vorticity Fourier coefficients α_o^{i+1}, α_n^{i+1}'s and β_n^{i+1}'s in R.

Equations (4.15)-(4.17) permit explicit evaluation of α_o^{i+1}, α_n^{i+1}'s and β_n^{i+1}'s using quadratures if $\alpha_o^i(1)$, $\alpha_n^i(1)$'s, $\beta_n^i(1)$'s and ξ_o^i, ξ_n^i's, ζ_n^i's, μ_n^i's, η_n^i's are known on the right hand side of these equations.

In the above iteration loop, it was found necessary to employ a point under-relaxation technique to obtain converged solutions. The new values of α_o^{i+1}, α_n^{i+1}'s and β_n^{i+1}'s in R are computed from

$$\alpha_o^{i+1} = \lambda_o \alpha_o^* + (1 - \lambda_o)\alpha_o^i \tag{4.23}$$

$$\alpha_n^{i+1} = \lambda \alpha_n^* + (1 - \lambda)\alpha_n^i \tag{4.24}$$

$$\beta_n^{i+1} = \lambda \beta_n^* + (1 - \lambda)\alpha_n^i \tag{4.25}$$

where $1 \leq n \leq N$, λ_o, λ are the under-relaxation parameter and α_o^*, α_n^*'s and β_n^*'s are the values computed in step (iv).

Converged solution of a particular problem is assumed to exist when the following criterion is satisfied.

$$D_{max} = \underset{j}{Max} \left| \alpha_{oj}^{i+1} - \alpha_{oj}^{i}, \alpha_{nj}^{i+1} - \alpha_{nj}^{1}, \beta_{nj}^{i+1} - \beta_{nj}^{i} \right| \leq \epsilon; \quad 1 \leq n \leq N \tag{4.26}$$

where subscript "j" denotes the Fourier coefficients at $r=r_j (r_j < 1)$. A good value for ϵ was found to be 10^{-4}.

The new numerical approach was tested and some of its features are discussed as the Reynolds number increases.

(i) <u>Flow without separation</u>

This is a closed streamline flow problem. The boundary velocities are:

$$v_{r_b} = 0 \tag{4.27}$$

$$v_{\theta_b} = \frac{1}{2} + \frac{1}{2}\cos\theta \qquad (4.28)$$

This example was treated by Burggraf (12). He used the Oseen approximation, which took a rigid-body rotation as the basic flow. The solution of such linearized differential equation is only applicable to the case in which the whole flow field forms a singular circular eddy. The asymptotic vorticity value of the inviscid core at high Re he obtained is too low compared to Batchelor's (13) suggested model, which is proven to be quite adequate by Imai (14) and the present calculations.

Using the present approach, converged solutions are obtained at different Reynolds numbers, from 0 to 1,000. The number of iterations, under-relaxation parameters and stream function values at the origin are presented in Table 6. The grid system is equivalent to 21 x 41 mesh points. The variation of maximum deviation D_{max} (in equation 4.22) versus the iteration number is shown in Figure 13 for Re = 1,000. In this case, the process of escalating the Reynolds number has not been used, i.e., the lower Reynolds number solution is not utilized as the initial solution to start the iteration procedure. This has otherwise been very effective in the calculations.

The computer time for each iteration is about 1 second. Compared with the computer time that Imai had used at different Reynolds numbers (14) this approach showed speedup by a factor 2 to 3.

The streamline patterns at Re = 0, 50, 300 are in Figure 14. The vorticity values at $\theta = 0$ with different Re are presented in Figure 15. As Re increases, the value of vorticity in the inviscid core eventually goes to the value suggested by Batchelor and Wood (13)*. Also in this figure,

* Wood actually calculated this value exactly after using the Von Mises transformation in the closed boundary layer region as $Re \to \infty$. Stated simply, the vorticity value in the inviscid core is determined by the root-mean-square speed of the closed boundary surface.

the boundary layer structure is clearly seen as the Reynolds number increases. Figure 16 shows the migration of the vortex center with increasing Reynolds number. It is clearly seen that the ultimate location of the vortex center for Re $\to\infty$ will be the center of the circle.

(ii) Flow consisting of two unsymmetric recirculating regions

This is also a flow with closed streamlines. The boundary conditions are

$$v_{r_b} = 0 \tag{4.29}$$

$$v_{\theta_b} = \frac{1}{3} + \frac{2}{3}\cos\theta \tag{4.30}$$

The streamlines and vorticity values at different Reynolds numbers are in Figure 17 and Figure 18. Notice that the asymptotic flow pattern for high Reynolds numbers cannot be found in a simple way as in the last example, since the form of the separation line is not known in advance.

(iii) Unflow - outflow problem

The flow problem together with the boundary velocities are depicted in Figure 19 In this case, the flow is symmetric about the x-axis, thus the Fourier expression could be simplified to

$$\omega = \sum_{n=1}^{N} \beta_n \sin n\theta \tag{4.31}$$

$$v_r = \sum_{n=1}^{N} a_n \cos n\theta \tag{4.32}$$

$$v_o = \sum_{n=1}^{N} q_n \sin n\theta \tag{4.33}$$

and

$$\omega v_r = \sum_{n=1}^{N} {}_n \sin n\theta \tag{4.34}$$

$$\omega v_\theta = \mu + \sum_{n=1}^{N} \mu_n \cos n\theta \tag{4.35}$$

Due to the velocity discontinuity at the boundary, a larger number of grid points is used in the agrimuthal direction. The grid system used in this case is equivalent to 21 x 81 mesh points in the whole plane. The 81 points along the circumferential direction were proven adequate. The use of 121 points in that direction generated differences of the streamfunction values less than 1 percent compared with the results that used 81 points. The effect of the grid size in radial direction has also been tested, as shown in Table 7. The computer time for each iteration, on the 21 x 81 grid system, is about 1.3 seconds, a CDC 6600.

The streamline patterns with different Reynolds numbers are depicted in Figure 20. The occurrence and growth of the separation bubble are clearly seen in this figure, as the Reynolds number increases.

Table 6

Re	λ_o	λ	ITER	ψ_o
0	.1	.1	3	.250
16	.1	.1	56	.256
32	.1	.1	51	.268
50	.1	.1	40	.279
75	.1	.1	62	.289
100	.1	.1	66	.293
128	.1	.1	128	.295
200	.01	.05	430	.296
300	.001	.01	475	.297
1000	.001	.001	4114	.289

Table 7

Re	Δr	λ, λ_o	ITER	ψ_{MAX}
100	.1	.2	47	.111
	.05	.1	80	.123
200	.1	.06	130	.116
	.05	.05	211	.132
300	.1	.03	230	.115
	.05	.002	440	.131

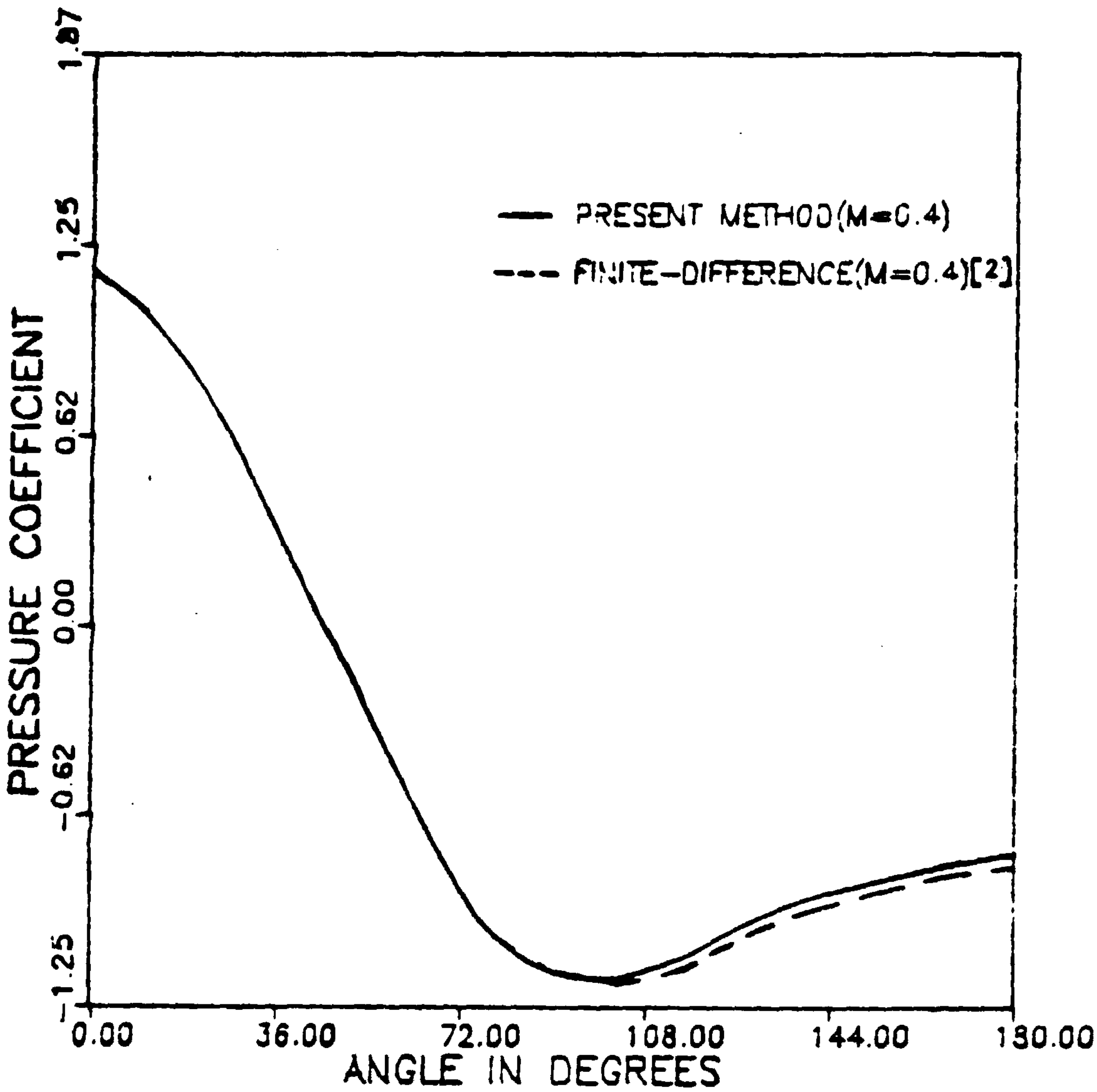

FIGURE (1) PRESSURE DISTRIBUTIONS ON CIRCULAR CYLINDER

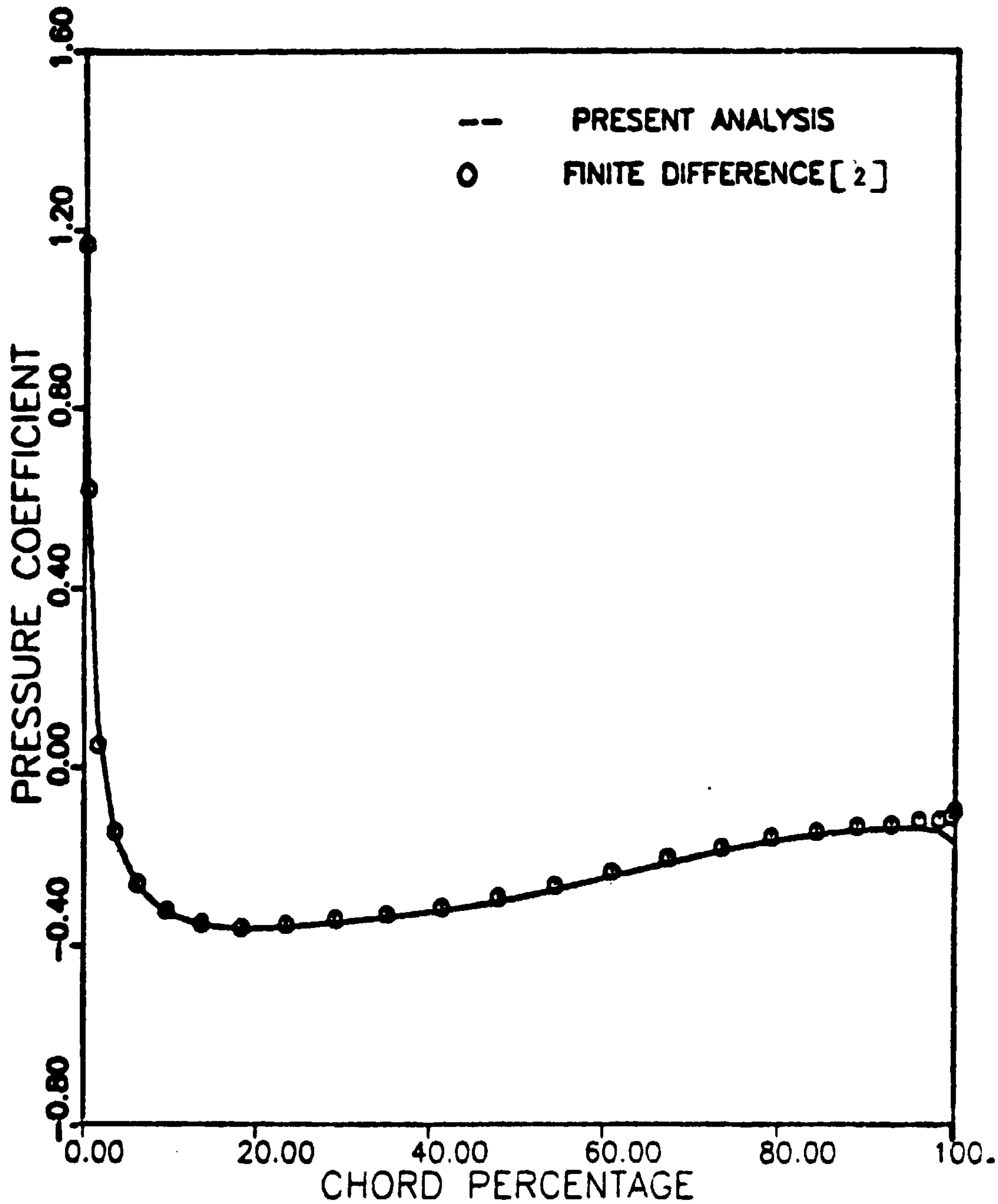

FIGURE(2) JOUKOWSKI 9% AIRFOIL AT ZERO ANGLE OF ATTACK

SURFACE PRESSURE DISTRIBUTION AT STEADY STATE

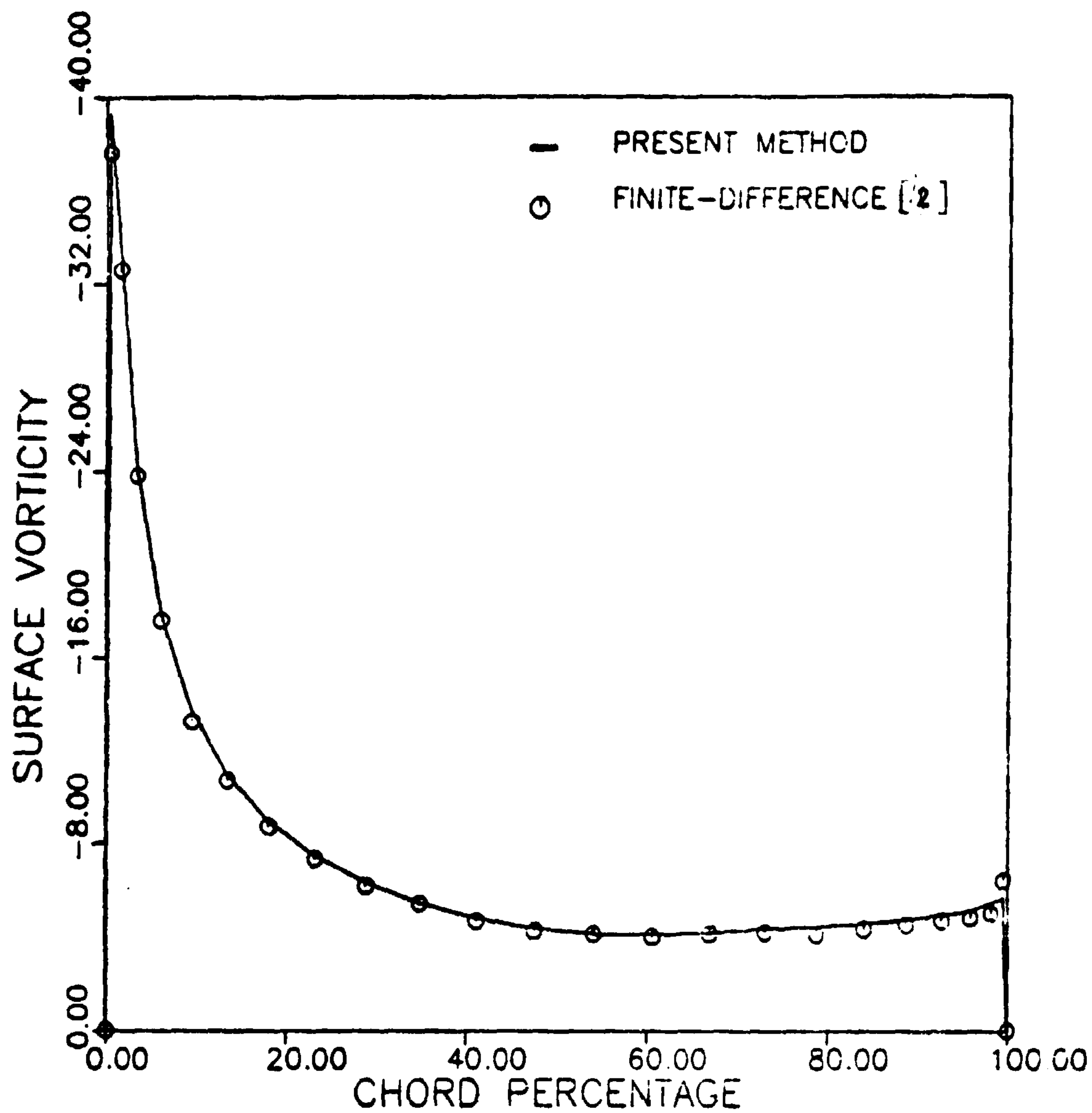

FIGURE(3) JOUKOWSKI 9% AIRFOIL AT ZERO ANGLE OF ATTACK--
SURFACE VORTICITY DISTRIBUTION AT STEADY STATE

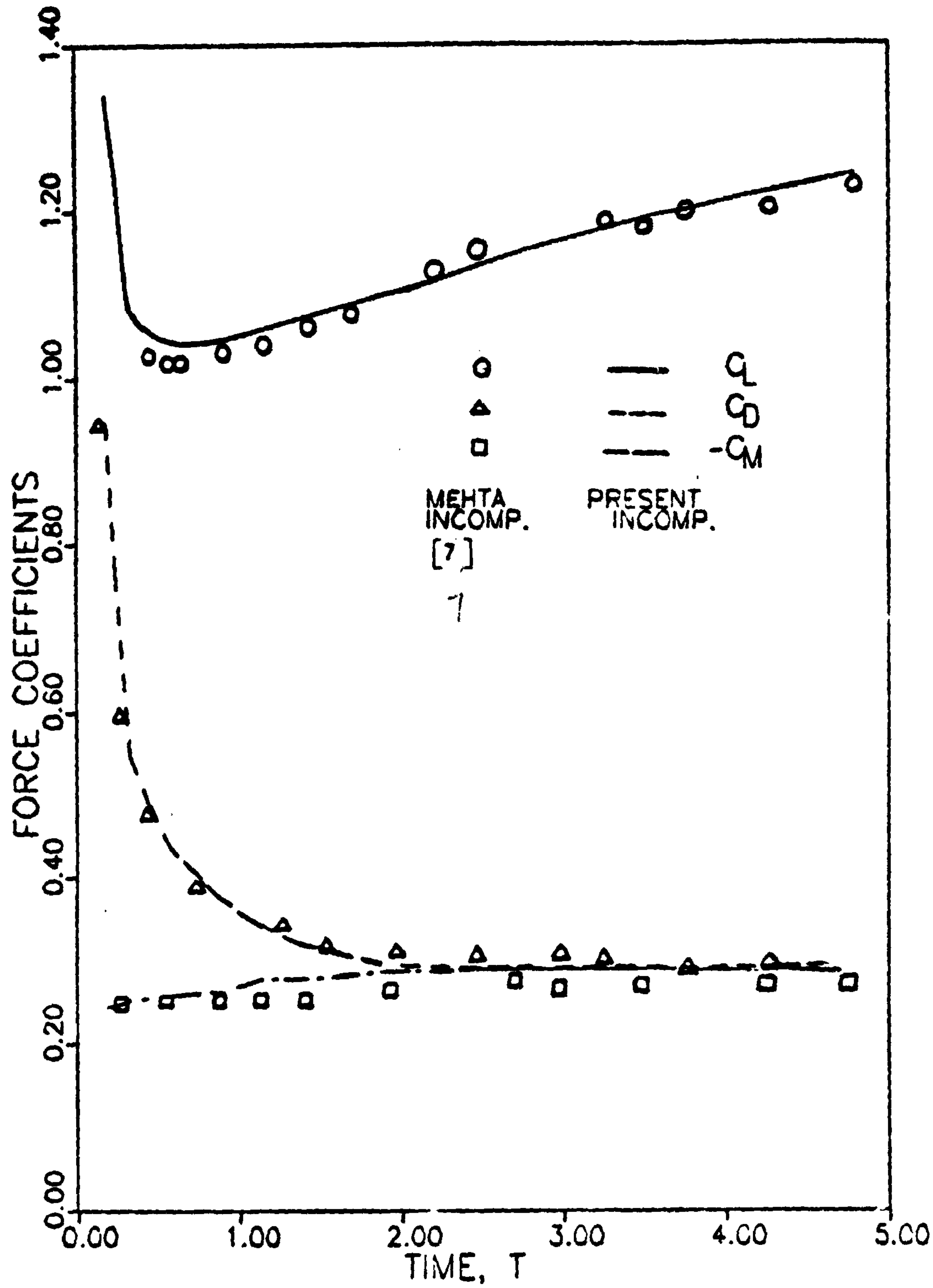

FIGURE (4) COMPARISON OF FORCE COEFFICIENTS BETWEEN THE PRESENT INCOMPRESSIBLE RESULTS AND THOSE OF REFERENCE

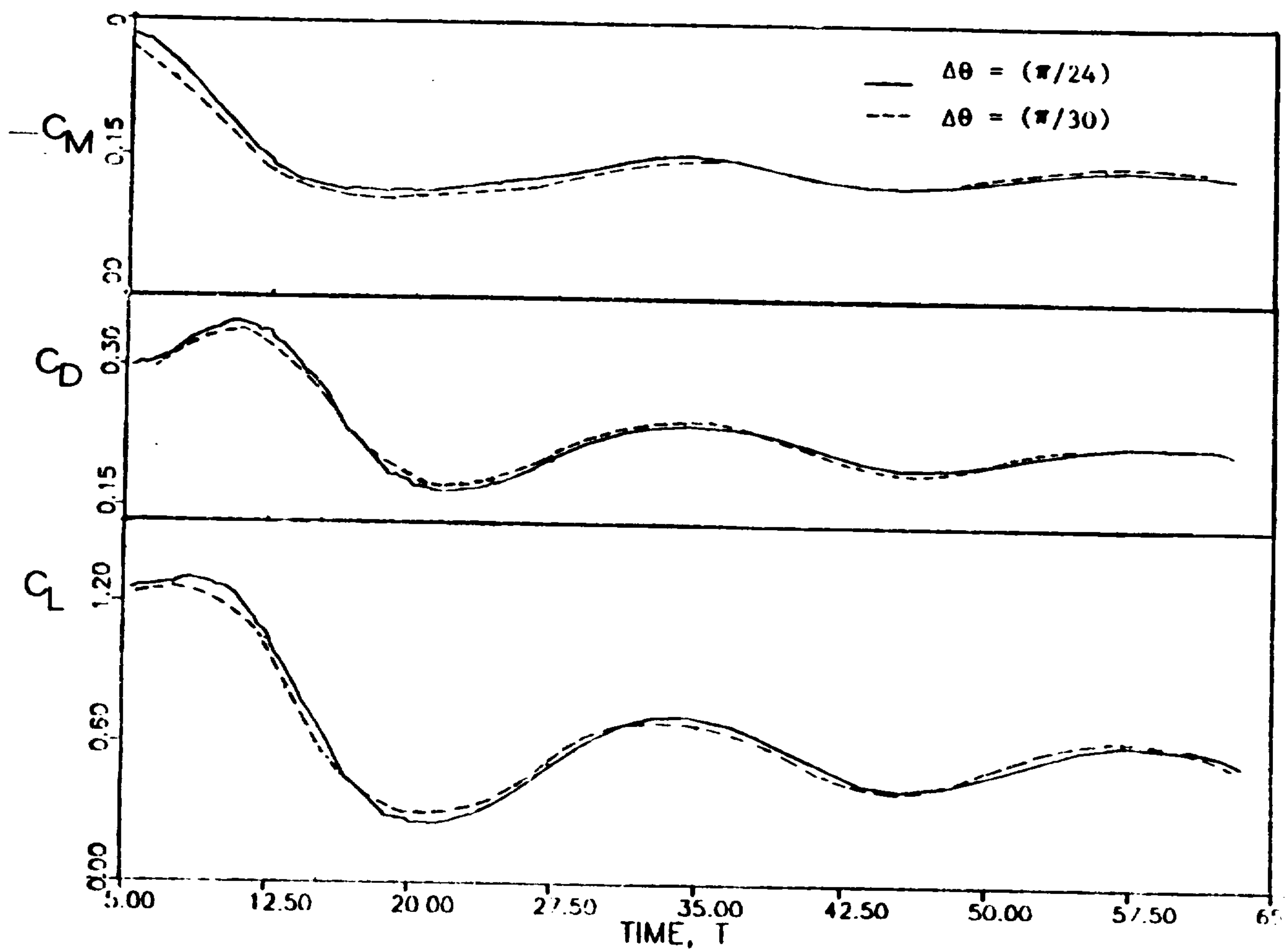

FIGURE(5). TIME HISTORIES OF LOADS

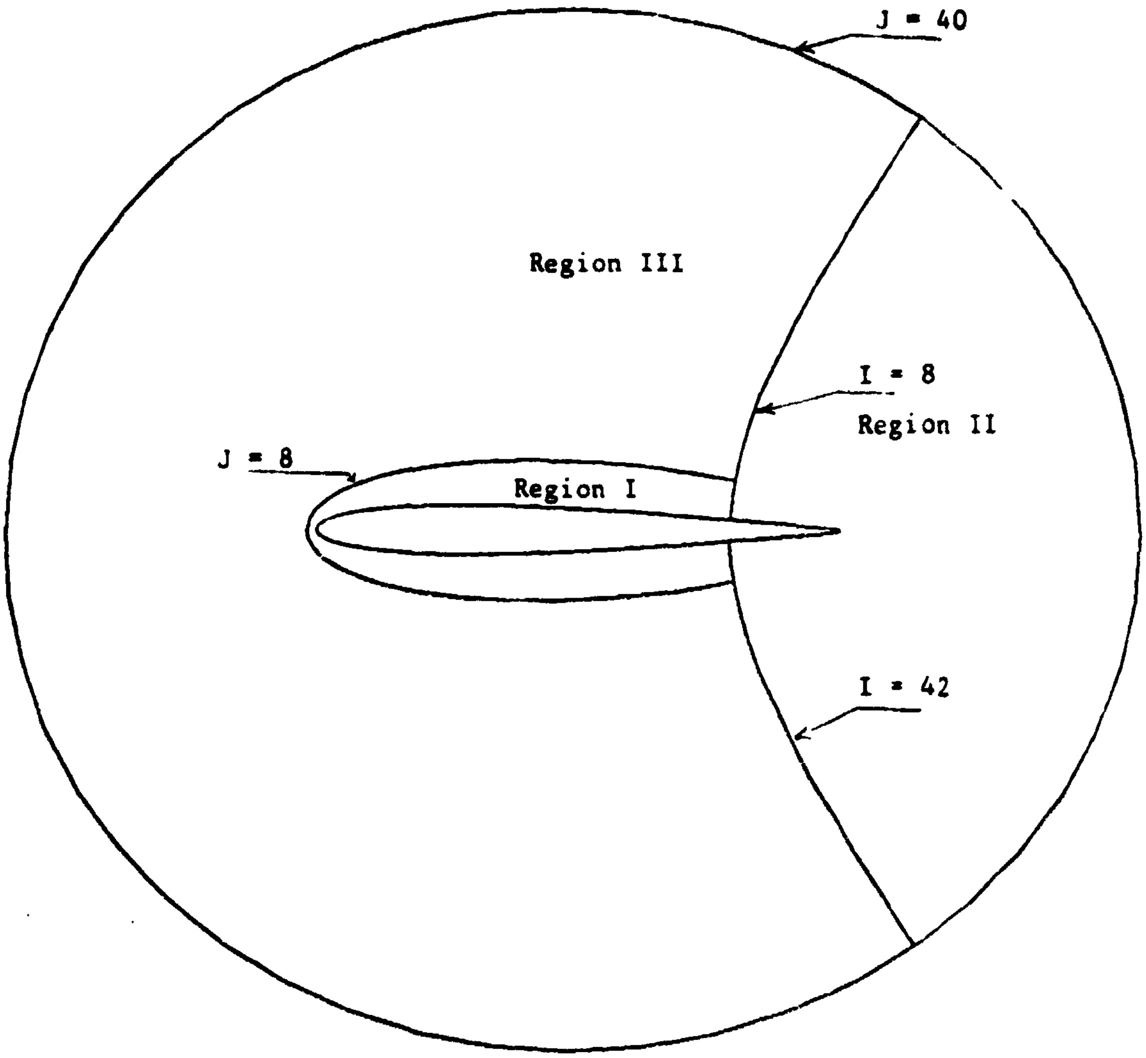

Region I The Integral Relation (3.30) is used to Calculate V_θ

Region II The Integral Relation (3.30) is used to Calculate V_θ

Region III Finite-Difference Equation (3.34) is used to Calculate V_θ

FIGURE (6) SEGMENTATION OF KINEMATICS AT LATE TIME LEVELS

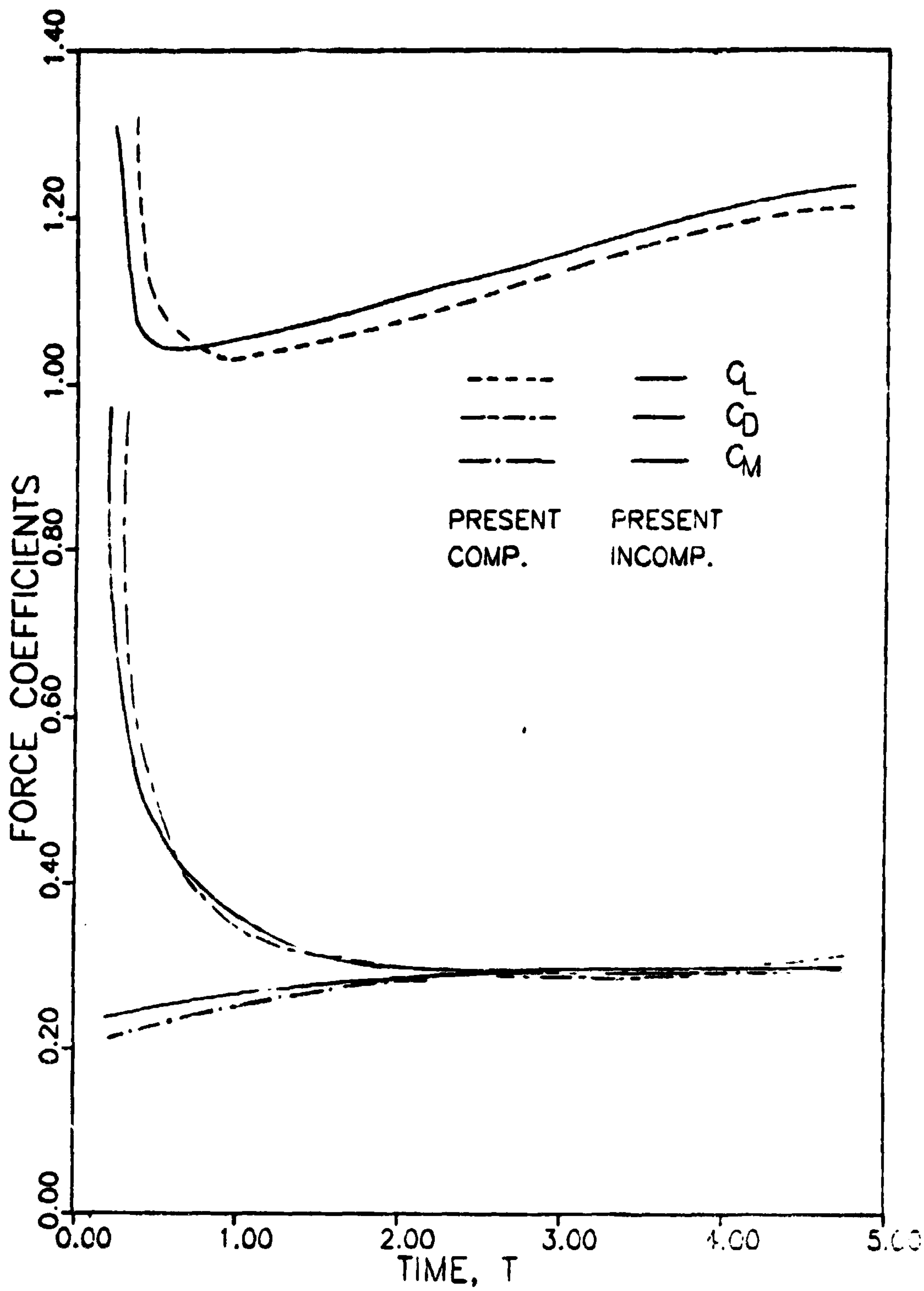

FIGURE(7) TIME HISTORIES OF LOADS , T=0. TO T=5.0

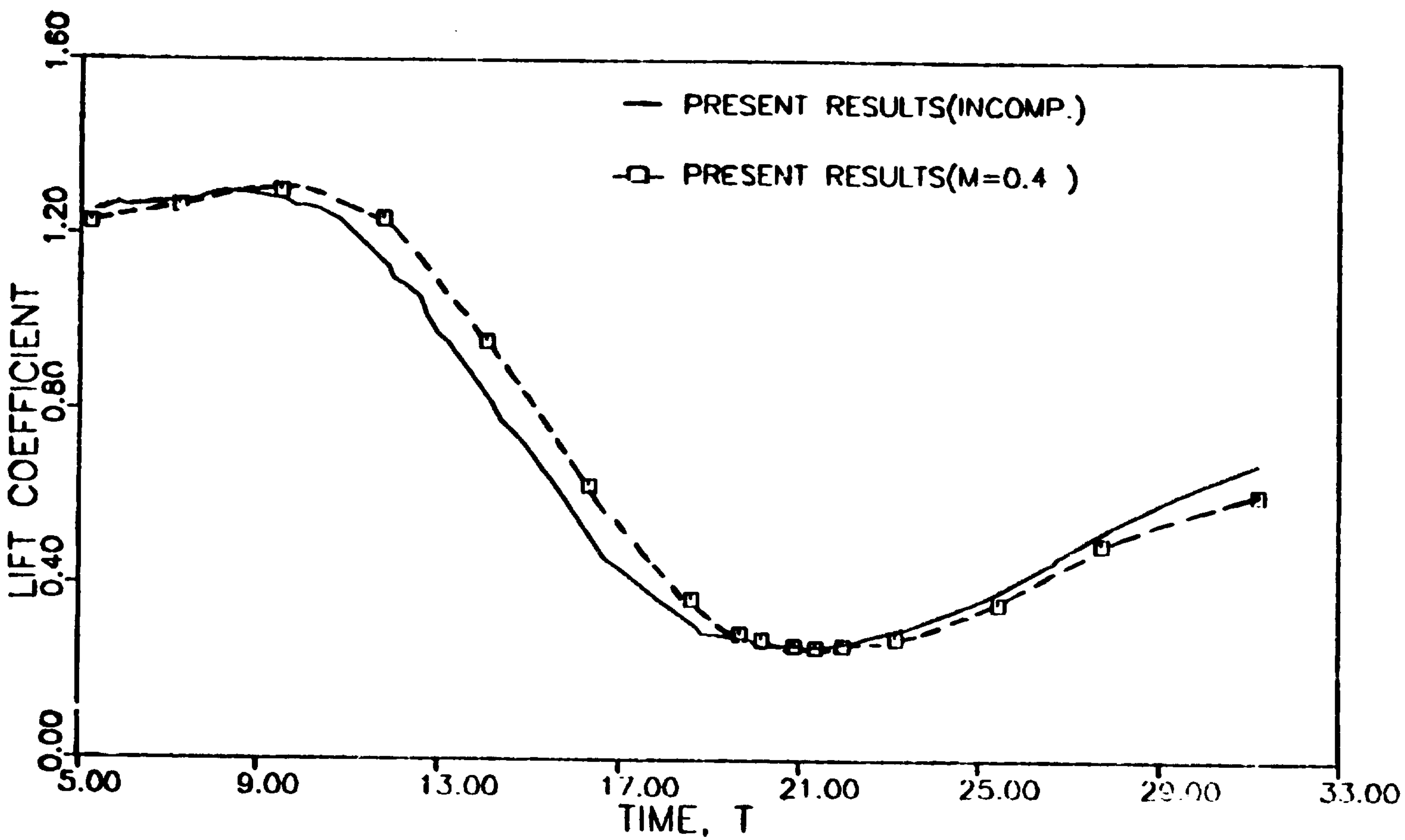

FIGURE(8) TIME HISTORIES OF LOADS

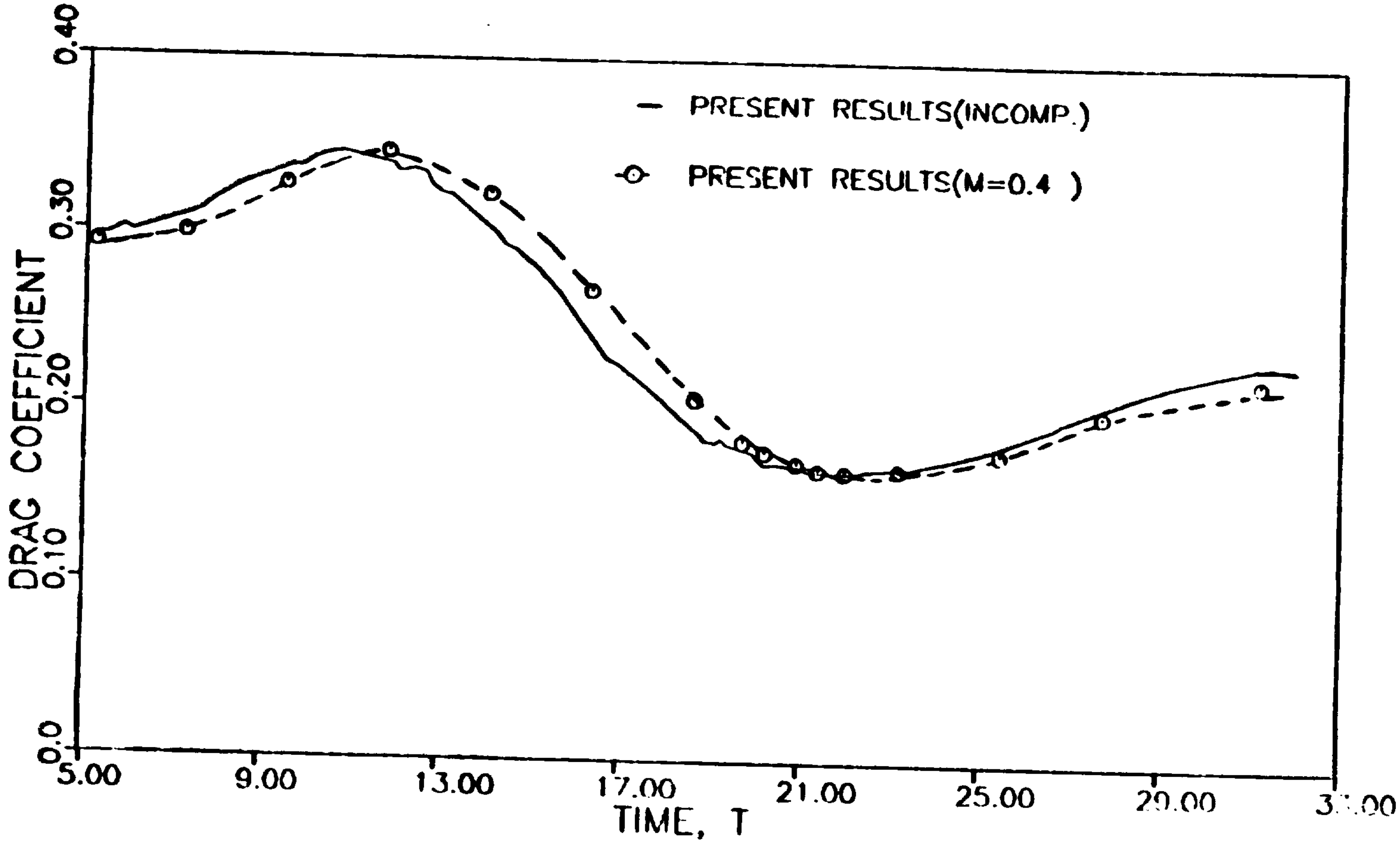

FIGURE(9). TIME HISTORIES OF LOADS

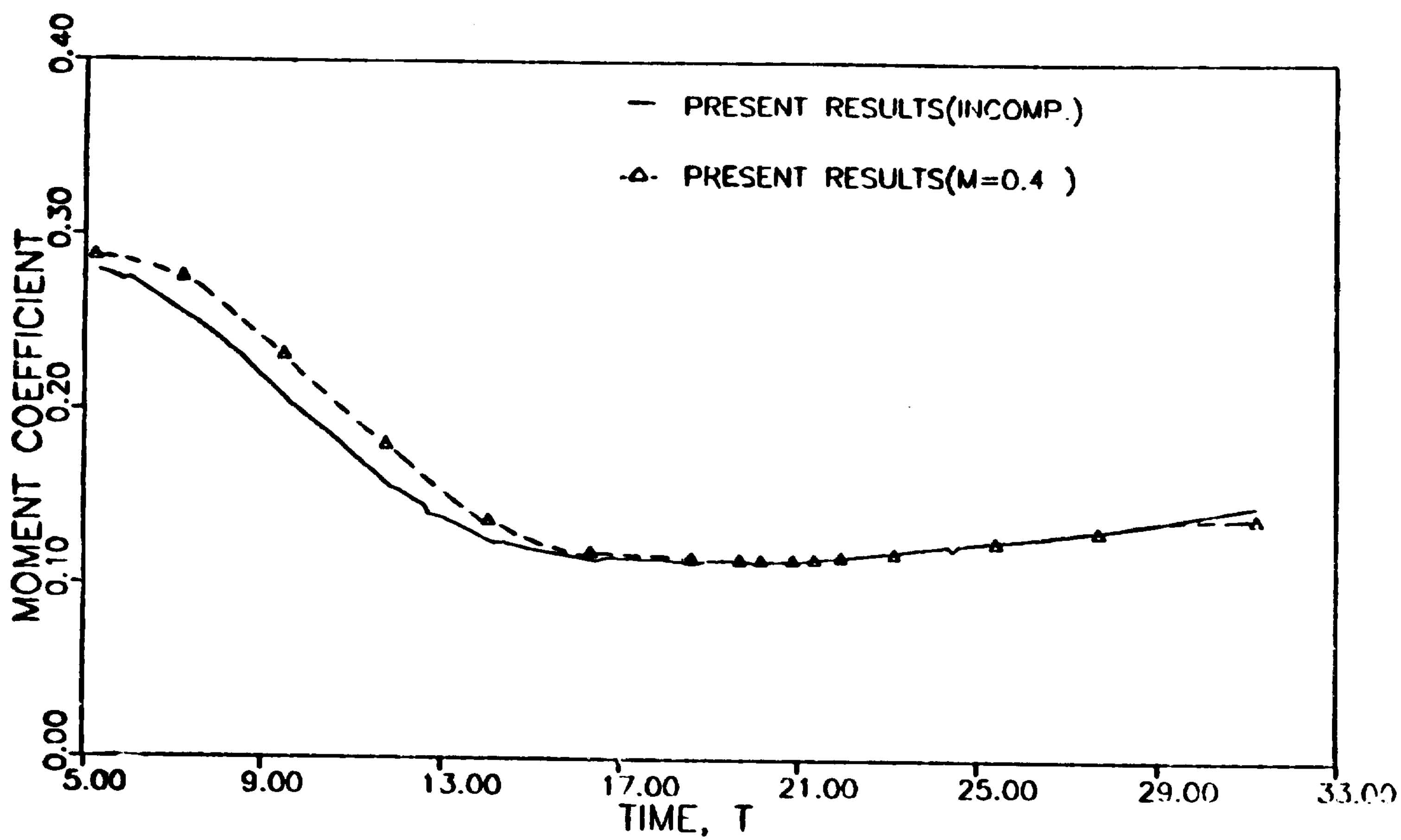

FIGURE(10) TIME HISTORIES OF LOADS

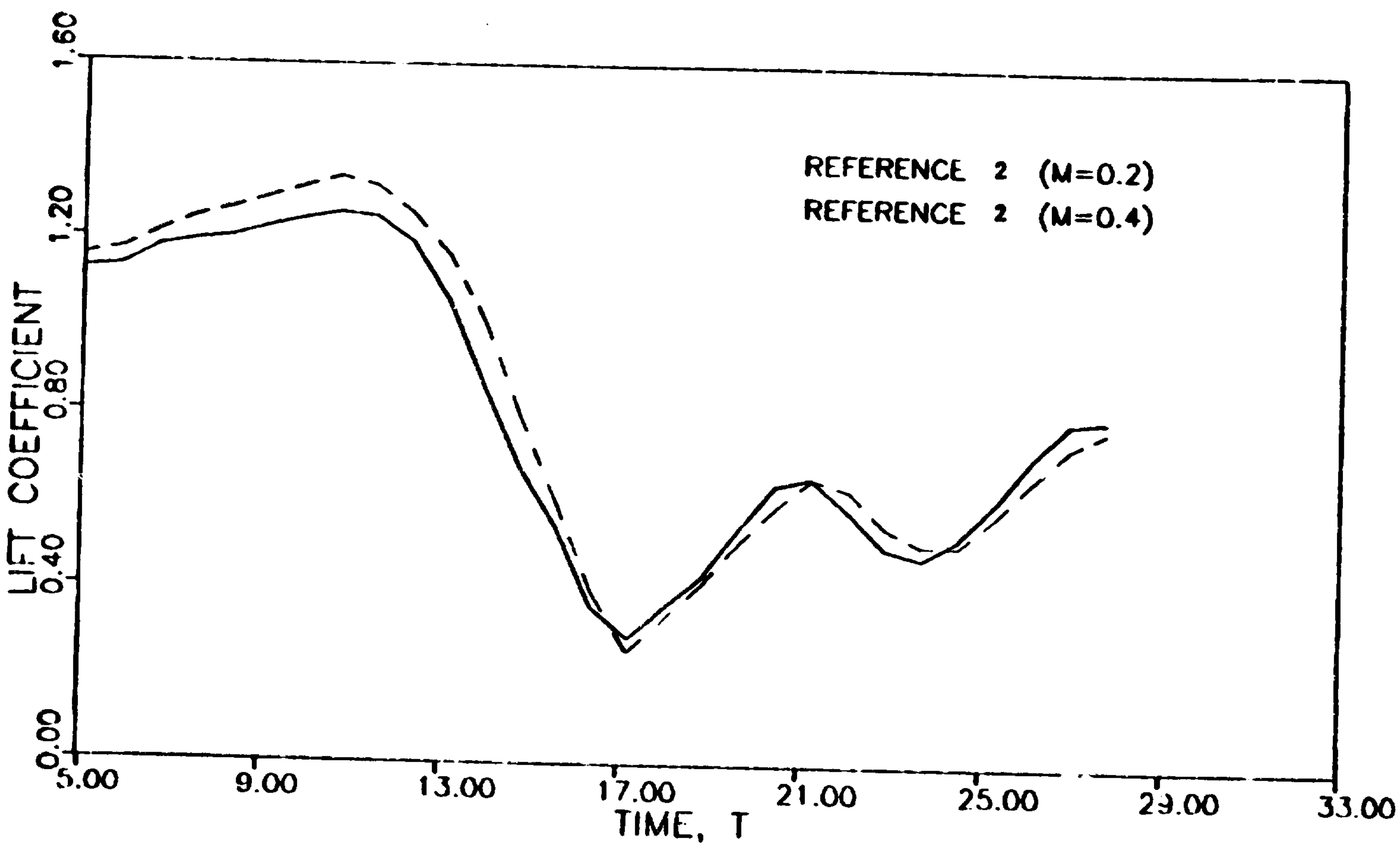

FIGURE(11) TIME HISTORIES OF LOADS

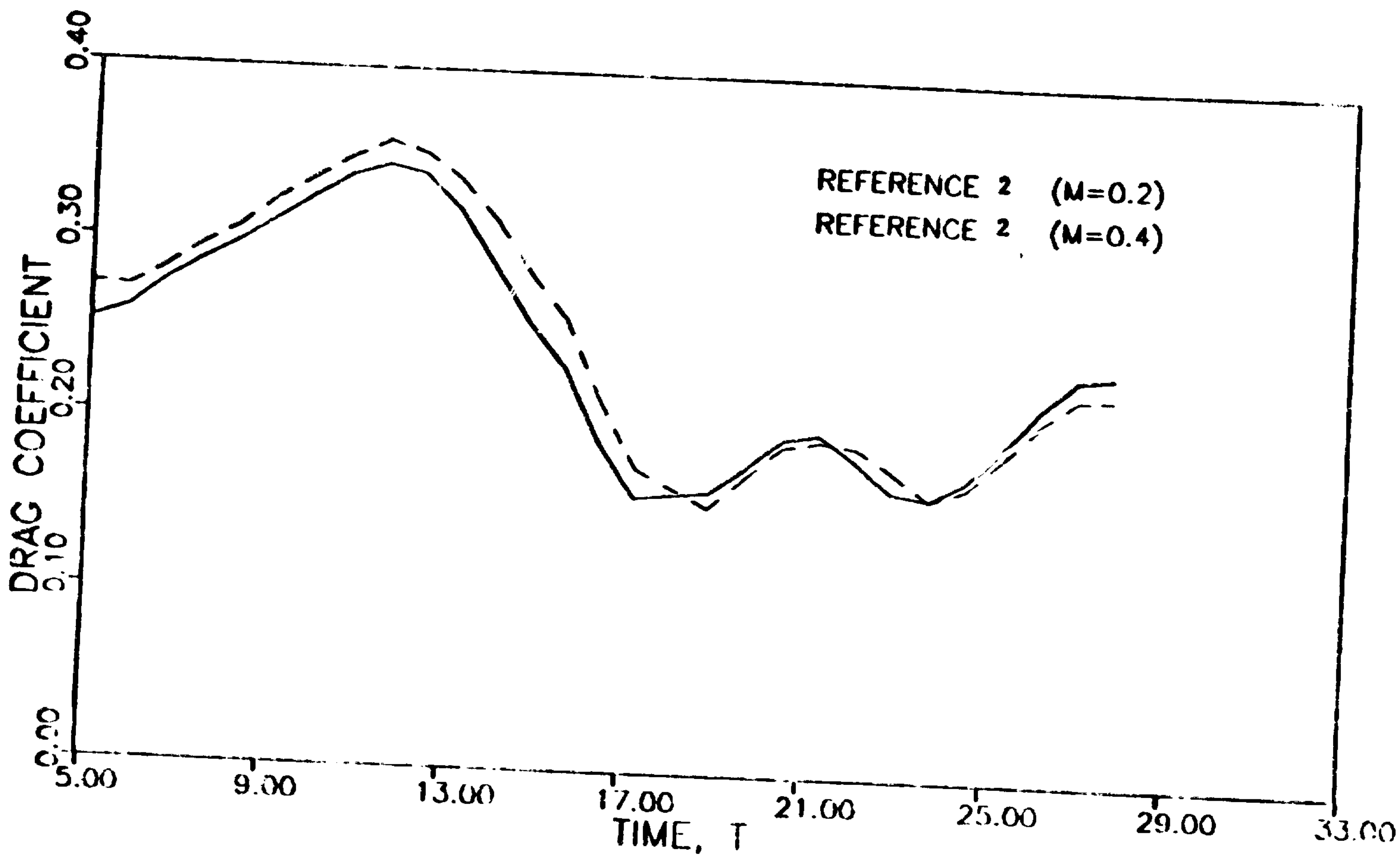

FIGURE(12) TIME HISTORIES OF LOADS

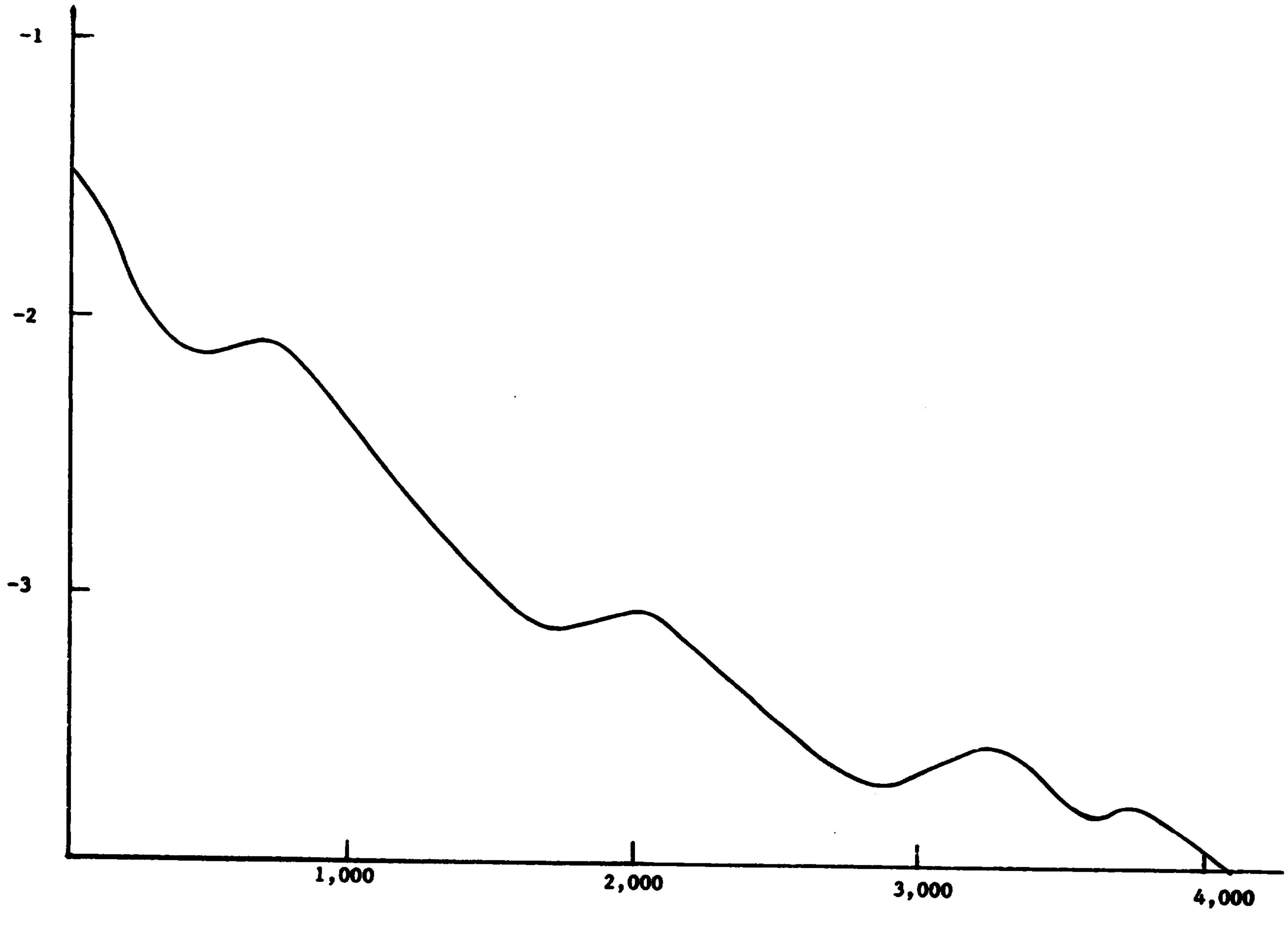

Figure 13

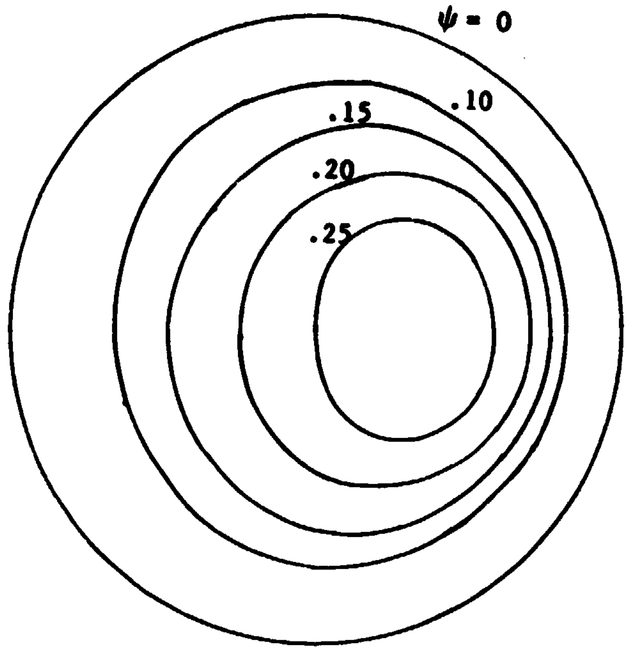

$R_e \to 0$

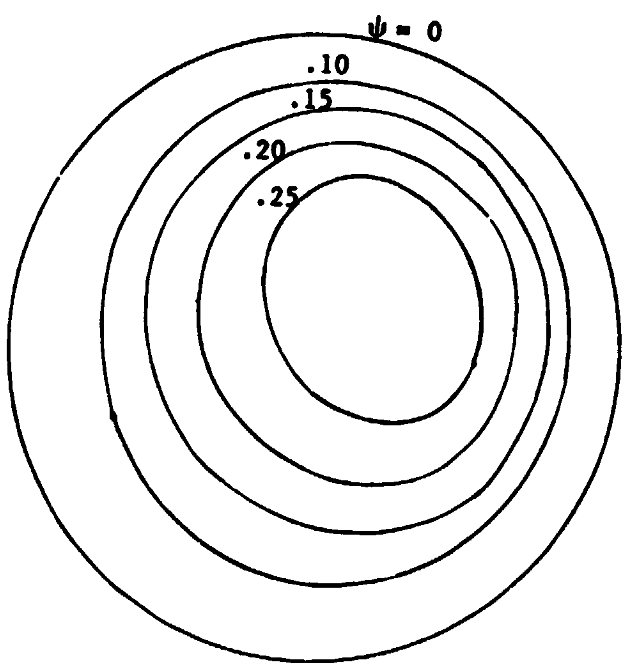

$R_e = 50$

Figure 14A

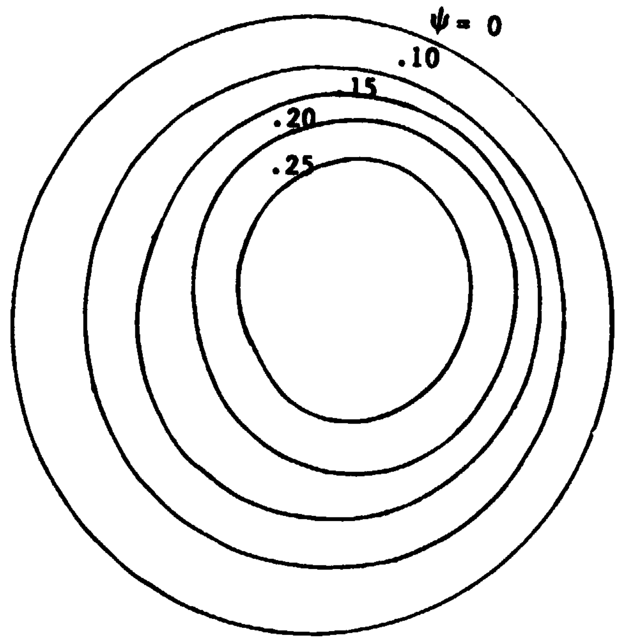

$R_e = 300$

Figure 14B

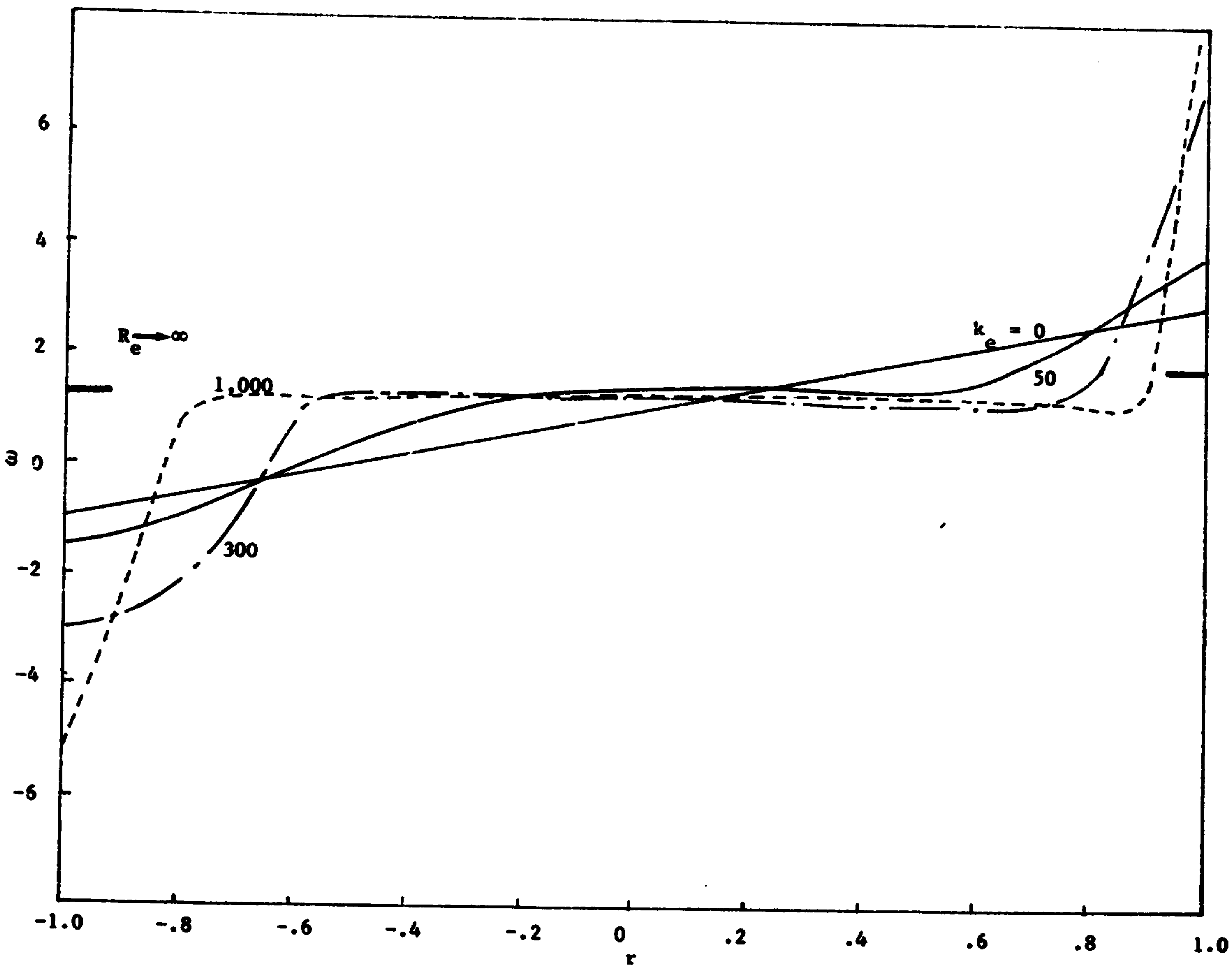

Figure 15

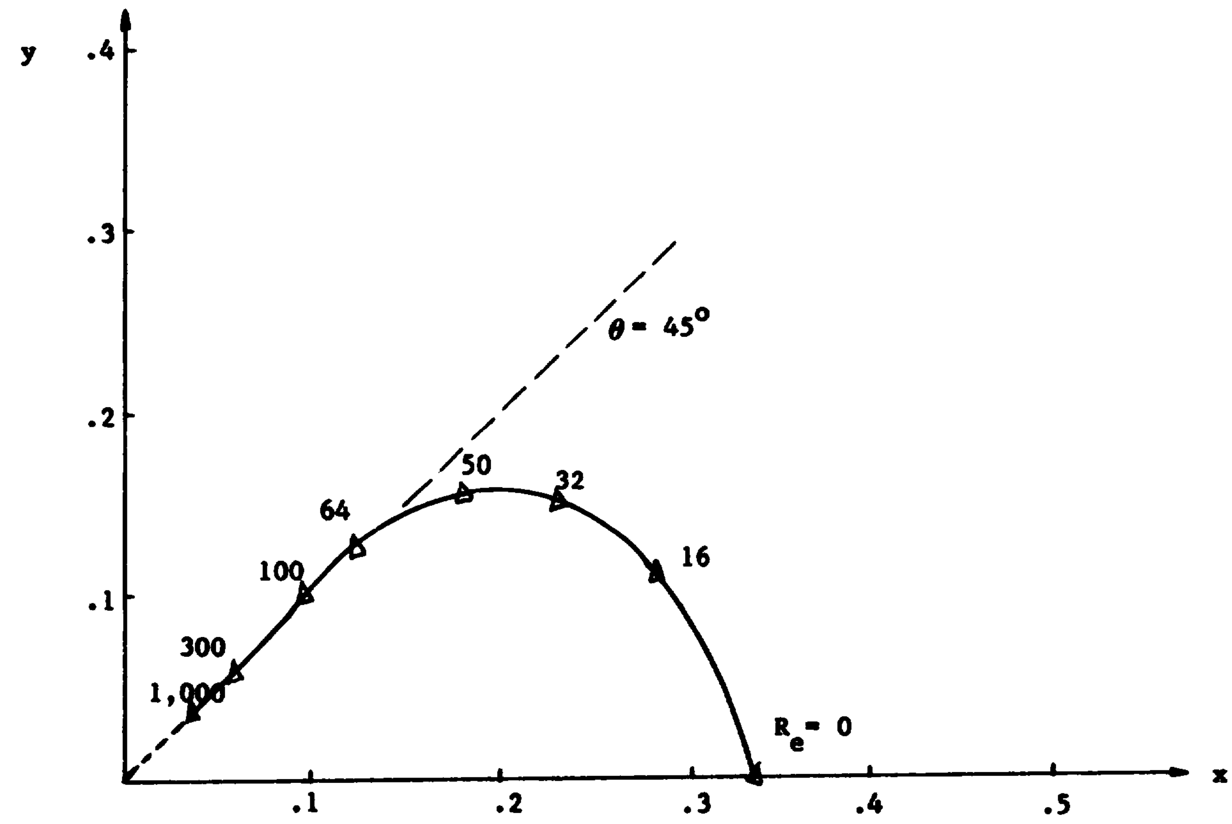

Figure 16

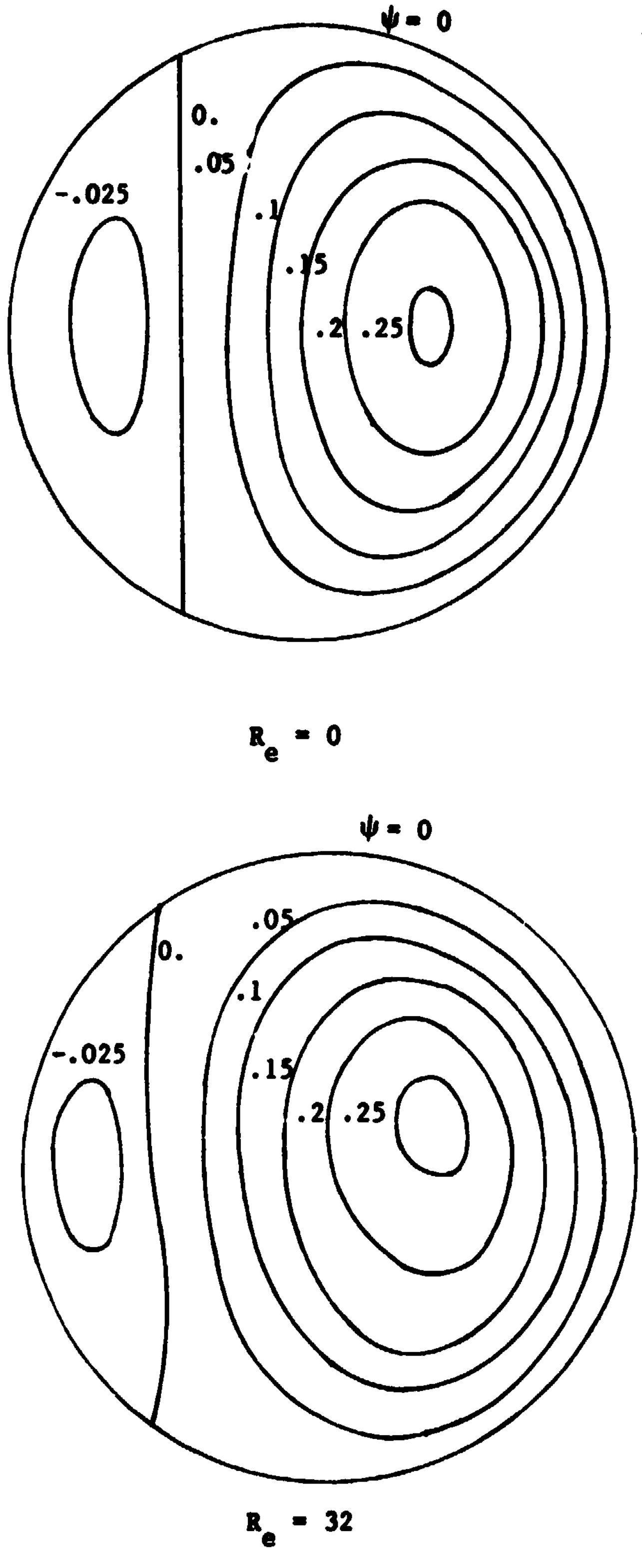

Figure 17A

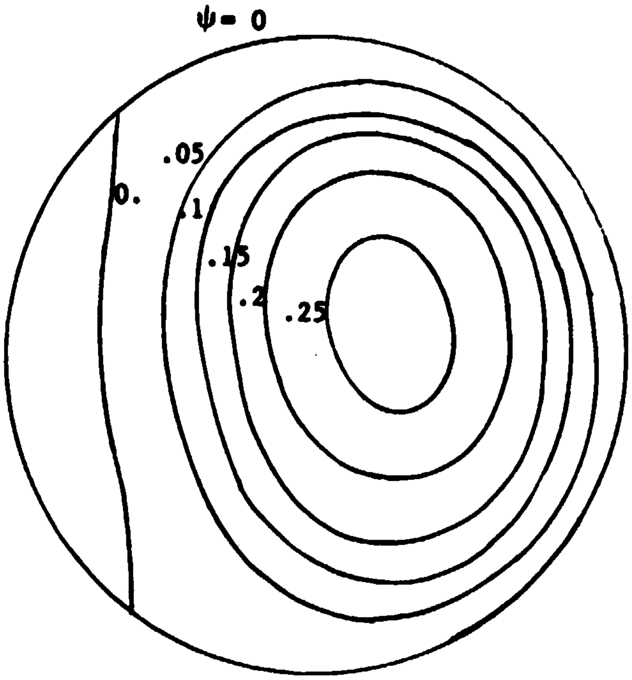

R_e = 200

Figure 17B

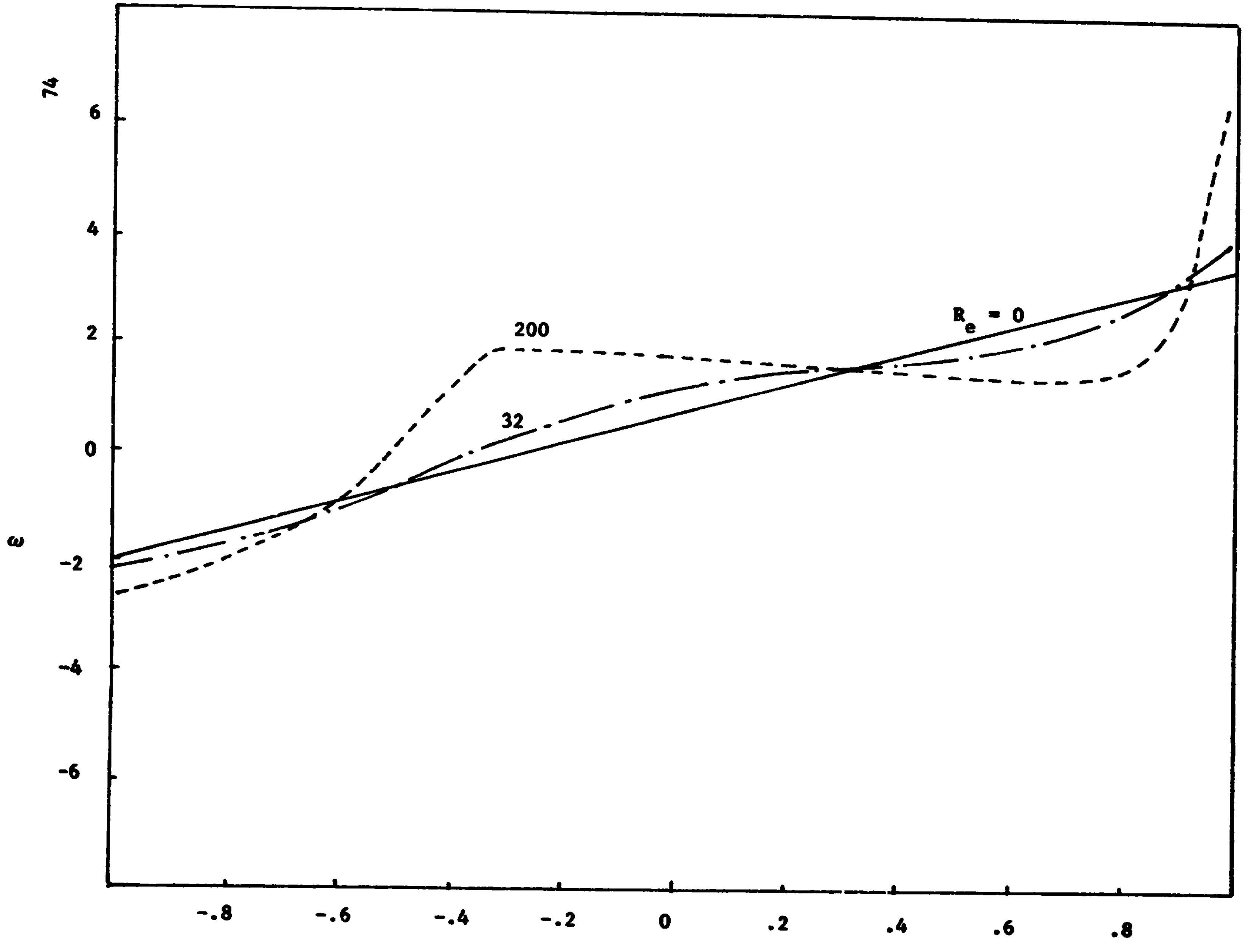

Figure 18

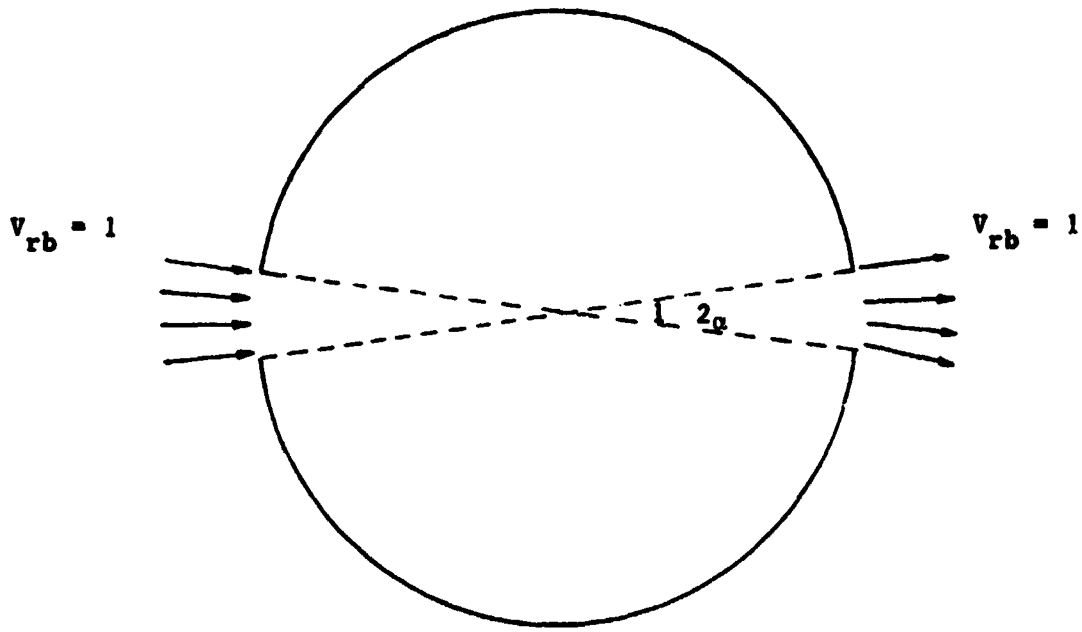

$$\alpha = 6^{\circ}$$

$$V_{\theta b} = 0$$

$$V_{rb} = \sum_{n=1}^{N} S_n(1) \cos\theta$$

$$S_n(1) = \frac{4}{n\pi} \sin n\alpha \quad n=1,3,5\ldots$$

$$S_n(1) = 0 \qquad n=0,2,4,\ldots$$

Figure 19

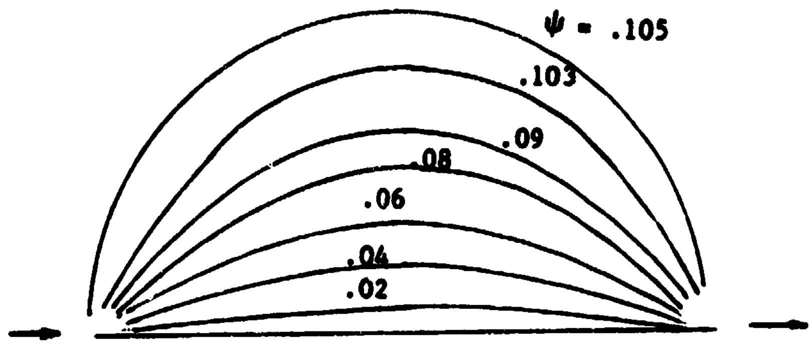

$R_e = 0$

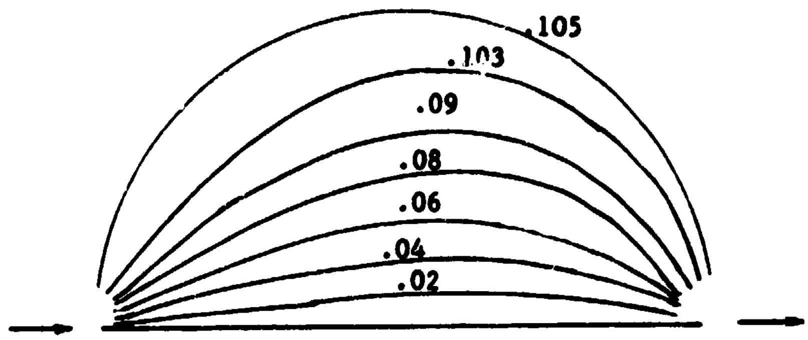

$R_e = 20$

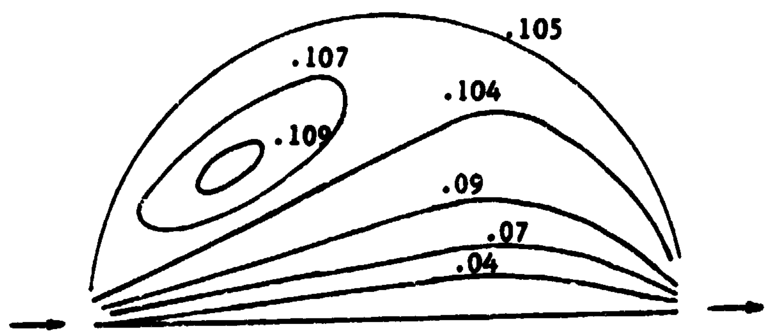

$R_e = 50$

Figure 20A

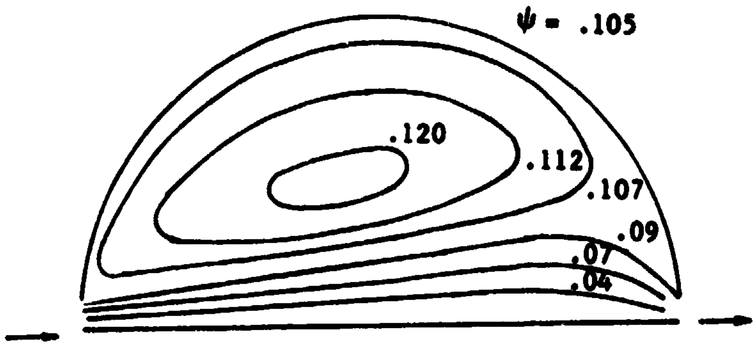

R_e = 100

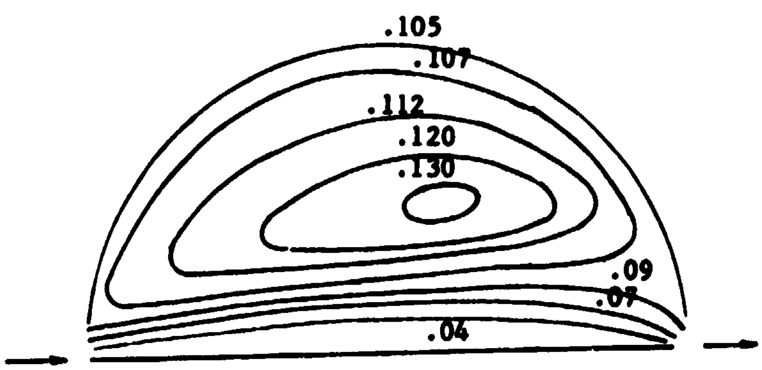

R_e = 300

Figure 20B

APPENDIX A

DERIVATION OF THE KINETIC TRANSPORT EQUATIONS

(1) The Vorticity Transport Equation

The vorticity transport equation (2.17) may be written as

$$\frac{\partial \omega}{\partial t} = \vec{\nabla} x (\vec{V} x \vec{\omega}) + \frac{(\gamma-1)}{\gamma} \vec{\nabla} \ln \rho x \vec{\nabla} h + \frac{1}{Re} \vec{\nabla} x (\frac{1}{\rho} \vec{\nabla} . \vec{\vec{\tau}}) \qquad (A.1)$$

For two-dimensional flow, we have

$$\vec{\nabla} x (\frac{1}{\rho} \vec{\nabla} . \vec{\vec{\tau}}) = \frac{\partial}{\partial x} (\frac{1}{\rho} \frac{\partial}{\partial x} (\mu \frac{\partial u}{\partial y} + \mu \frac{\partial v}{\partial x}) + \frac{1}{\rho} \frac{\partial}{\partial y} (2\mu \frac{\partial v}{\partial y} - \frac{2}{3} \mu \beta)$$

$$- \frac{\partial}{\partial y} (\frac{1}{\rho} \frac{\partial}{\partial x} (2\mu \frac{\partial u}{\partial x} - \frac{2}{3} \mu \beta) \quad \text{[illegible]} \frac{\partial}{\partial y} (\mu \frac{\partial u}{\partial y} + \mu \frac{\partial v}{\partial x}) \qquad (A.2)$$

and

$$\vec{\nabla} x (\vec{v} x \vec{\omega}) = - (\vec{V} . \vec{\nabla} \vec{\omega} + \omega \beta) = - \vec{\nabla} . (\vec{V} \omega) \qquad (A.3)$$

Upon differentiating the terms in equation (A-2) it reduces to

$$\vec{\nabla} x (\frac{1}{\rho} \vec{\nabla} . \vec{\vec{\tau}}) = T_1 + T_2 \qquad (A.4)$$

where T_1 represents the summation of the free-viscosity change terms and T_2 represents the terms which include the change of viscosity.

$$T_1 = \frac{-1}{\rho^2}\frac{\partial\rho}{\partial x}\left(\mu\frac{\partial^2 u}{\partial x\partial y} + \mu\frac{\partial^2 v}{\partial x^2}\right) + \frac{1}{\rho^2}\frac{\partial\rho}{\partial y}\left(\mu\frac{\partial^2 u}{\partial y^2} + \mu\frac{\partial^2 v}{\partial x\partial y}\right) + \frac{\mu}{\rho}\nabla^2\omega$$

$$- \frac{1}{\rho^2}\frac{\partial\rho}{\partial x}\left(2\mu\frac{\partial^2 v}{\partial y^2} - \frac{2}{3}\mu\frac{\partial\beta}{\partial y}\right) + \frac{1}{\rho^2}\frac{\partial\rho}{\partial y}\left(2\mu\frac{\partial^2 u}{\partial x^2} - \frac{2}{3}\mu\frac{\partial\beta}{\partial x}\right) \qquad (A.5)$$

and

$$T_2 = \frac{1}{\rho}(u_y + v_x)(\mu_{xx} - \mu_{yy}) + \frac{2}{\rho}(v_y - u_x)\mu_{xy}$$

$$+ \mu_x\left(\frac{2}{\rho}\nabla^2 v + \frac{2}{\rho}u_{xy} - \frac{1}{\rho^2}(\rho_x u_y + v_x\rho_x - 2\rho_y u_x + \frac{2}{3}\rho_y\beta\right)$$

$$+ \mu_y\left(-\frac{2}{\rho}\nabla^2 u + \frac{2}{\rho}v_{xy} - \frac{1}{\rho^2}(2\rho_x v_y - u_y\rho_y - v_x\rho_y - \frac{2}{3}\beta\rho_x\right) \qquad (A.6)$$

For simplicity and convenience, the viscosity coefficients μ and $\lambda(\lambda = -\frac{2}{3}\mu)$, specific heat radio Υ and the thermal conductivity k have been considered to be constant in the present subsonic study. In general, the incorporation of variable coefficients has no conceptual effect on the method. Several numerical experiments have been performed to verify the foregoing assumption and the results indicate a negligible contribution of the non-constant coefficient term T_2.

By using the above assumptions, equation (A.6) reduces to the following simple form:

$$\frac{\partial\omega}{\partial t} = -\vec{\nabla}.(\vec{V}\omega) + \left(\frac{\mu}{\rho.Re}\right)\nabla^2\omega + \phi(\omega,\beta,\rho,h) \qquad (A.7)$$

where,

$$\phi = \phi_1 + \phi_2$$

$$\phi_1 = \frac{\mu}{Re.\rho^2}\left(\frac{4}{3}(\vec{\nabla}\beta \times \vec{\nabla}\rho).\vec{k} - \vec{\nabla}\rho.\vec{\nabla}\omega\right)$$

$$\phi_2 = \frac{\gamma-1}{\gamma}(\vec{\nabla}\ln \times \vec{\nabla}h).\vec{k}$$

$\vec{k}$ is the unit vector normal to the plane of flow (x-y).

(2) <u>The Dilatation Transport Equation</u>

The dilatation transport equation (2-18) may be written as

$$\frac{\partial\delta}{\partial t} = -\vec{\nabla}.(\vec{V}.\vec{\nabla})\vec{V} - \frac{\gamma-1}{\gamma}\nabla^2 h - \frac{\gamma-1}{\gamma} h\,\nabla^2\ln\rho - \frac{\gamma-1}{\gamma}\vec{\nabla}\ln\rho.\vec{\nabla}h$$

$$+ \frac{1}{Re}\vec{\nabla}.(\frac{1}{\rho}\vec{\nabla}.\vec{\vec{\tau}}) \qquad \text{(A.8)}$$

Specializing this for two-dimensional flow and expanding the first and the last term in the right-hand side, one obtain:

$$-\vec{\nabla}.(\vec{V}.\vec{\nabla})\vec{V} = -\frac{\partial}{\partial x}(u\frac{\partial u}{\partial x} + v\frac{\partial u}{\partial y}) - \frac{\partial}{\partial y}(u\frac{\partial v}{\partial x} + v\frac{\partial v}{\partial y})$$

$$-(u\frac{\partial^2 v}{\partial x\partial y} + \frac{\partial v}{\partial x}.\frac{\partial u}{\partial y} + (\frac{\partial v}{\partial y})^2 + v\frac{\partial^2 v}{\partial y^2})$$

$$-(u\frac{\partial^2 u}{\partial x^2} + \frac{\partial v}{\partial x}.\frac{\partial u}{\partial y} + (\frac{\partial u}{\partial x})^2 + v\frac{\partial^2 v}{\partial x\partial y}) \qquad \text{(A.9)}$$

Further, noting that,

$$\beta = \frac{\partial u}{\partial x} + \frac{\partial v}{\partial y}$$

Equation (A.9) reduces to the following form

$$-\vec{\nabla}.(\vec{V}.\vec{\nabla})\vec{V} = -(u\,\frac{\partial\beta}{\partial x} + v\,\frac{\partial\beta}{\partial y} + u_x^2 + v_y^2 + 2v_x\,u_y) \qquad \text{(A.10)}$$

Equation (A.10) can be further reduced to

$$-\vec{\nabla}.(\vec{V}.\vec{\nabla})\vec{V} = -(u\,\frac{\partial\beta}{\partial x} + v\,\frac{\partial\beta}{\partial y} + \beta^2 + 2\vec{\nabla}v x\vec{\nabla}u.\vec{k})$$

$$= -\,(\vec{\nabla}.(\vec{V}\beta) + 2\vec{\nabla}v x\vec{\nabla}u.\vec{k}) \qquad \text{(A.11)}$$

Similarly,

$$\vec{\nabla}.(\frac{1}{\rho}\,\vec{\nabla}.\vec{\tau}) = \frac{\partial}{\partial x}\,(\frac{1}{\rho}\,(\frac{\partial}{\partial x}\,(2\mu\,\frac{\partial u}{\partial x} - \frac{2}{3}\,\mu\beta) + \frac{\partial}{\partial y}\,(\mu\,\frac{\partial u}{\partial y} + \mu\,\frac{\partial v}{\partial x})))$$

$$+ \frac{\partial}{\partial y}\,(\frac{1}{\rho}\,(\frac{\partial}{\partial x}\,(\mu\frac{\partial u}{\partial y} + \mu\,\frac{\partial v}{\partial x}) + \frac{\partial}{\partial y}\,(2\mu\,\frac{\partial v}{\partial y} - \frac{2}{3}\,\mu\beta))) \qquad \text{(A.12)}$$

By separating the right-hand side into two terms, similar to what has been done in the vorticity transport equation, one obtains

$$\vec{\nabla}\,.(\frac{1}{\rho}\,\vec{\nabla}.\vec{\tau}) = C_1 + C_2 \qquad \text{(A.13)}$$

where

$$C_1 = \frac{4}{3}\frac{\mu}{\rho}\nabla^2\beta - (\frac{4}{3}\frac{\mu}{\rho^2}\vec{\nabla}\rho.\vec{\nabla}\beta + \frac{\mu}{\rho^2}(\vec{\nabla}\rho x\vec{\nabla}\omega).\vec{k} \tag{A.14}$$

$$C_2 = (\frac{8}{3}\rho)\ \vec{\nabla}\beta.\vec{\nabla}\mu + \frac{2}{3}(\vec{\nabla}\omega x\vec{\nabla}\mu).\vec{k} - (\frac{2}{3}\rho)\beta\nabla^2\mu$$

$$+ (\frac{2}{\rho})\ (u_x\ \ _{xx} + v_y\ \mu_{yy}) + (v_x + u_y)\mu_{xy}$$

$$- (\frac{1}{\rho^2})(v_x + u_y)\ (\rho_x.\mu_y + \rho_y\ .\mu_x) + (\frac{2}{3})\ \frac{\beta}{\rho^2}\ \vec{\nabla}\rho.\vec{\nabla}\mu$$

$$- (\frac{2}{\rho^2})\ (\rho_x.u_x.\mu_x + \rho_y\ .\ V_y.\ \mu_y) \tag{A.15}$$

Neglecting the term C_2, for the reasons mentioned before in (1), the dilatation transport equation is written as follows

$$\frac{\partial\beta}{\partial t} = -\vec{\nabla}.(\vec{V}\beta) + (\frac{4.\mu}{3.Re\rho})\ \nabla^2\beta + \chi(\omega,\beta,\rho,h) \tag{A.16}$$

where

$$\chi = \chi_1 + \chi_2 + \chi_3$$

$$\chi_1 = -2\ (\vec{\nabla}v\ x\ \vec{\nabla}u).\vec{k}$$

$$\chi_2 = \frac{\mu}{\rho^2 Re}\left\{-\frac{4}{3}\vec{\nabla}\rho\cdot\vec{\nabla}\beta + (\vec{\nabla}\rho\, x\, \vec{\nabla}\omega).\vec{k}\right\}$$

$$\chi_3 = -(\frac{\gamma-1}{\gamma})\ (\nabla^2 h + h\nabla^2 \ln\rho + \vec{\nabla}h.\vec{\nabla}\ln\rho)$$

(3) <u>The Energy Transport Equation</u>

Using the equation of state (2.4) in the energy equation (2.3), one obtains the following

$$\frac{\partial h}{\partial t} = -\vec{V}.\vec{\nabla}h - (\gamma-1)\beta h - \frac{\gamma}{\rho}\,\vec{\nabla}.\vec{q} + \frac{\gamma}{\rho}\,(\vec{\nabla}\vec{V}:\vec{\tau}) \tag{A.17}$$

Equation (A.17) can be written in dimensionless form as follows

$$\frac{\partial h}{\partial t} = -\vec{V}.\vec{\nabla}h - (\gamma-1)\beta h - \frac{\gamma}{\rho}\,\frac{1}{Re.Pr}\,\vec{\nabla}.\vec{q} + \frac{\gamma}{\rho.Re}\,(\vec{\nabla}\vec{V}:\vec{\tau}) \tag{A.18}$$

Expanding the conductive and dissapative terms in equation (A.18) one gets the following expressions

$$\frac{\gamma}{\rho Re.Pr}\,\vec{\nabla}.\vec{q} = \frac{\gamma}{\rho}\,\frac{1}{Re.Pr}\,\frac{\partial}{\partial x_j}\,(-k_j\,\frac{\partial h}{\partial x_j}) \tag{A.19}$$

and

$$\frac{\gamma}{\rho}\,\frac{1}{Re}\,(\vec{\nabla}\vec{V}:\vec{\tau}) = \frac{\gamma}{\rho.Re}\,(\tau_{ij}\,\frac{\partial u_i}{\partial x_j}) \tag{A.20}$$

Specializing these two equations for two-dimensional flow, they reduce to:

$$\frac{\gamma}{\rho Re.Pr}\,\vec{\nabla}.\vec{q} = \frac{\gamma}{\rho}\,(\frac{1}{Re.Pr})\,(k\,\nabla^2 h + \vec{\nabla}h.\vec{\nabla}k) \tag{A.21}$$

and

$$\frac{\gamma}{\rho}\frac{1}{Re}\vec{\nabla}\vec{V}:\vec{\tau} = \frac{\gamma\mu}{\rho.Re}\left(\frac{4}{3}\beta^2+\omega^2 + 4(\vec{\nabla}v \times \vec{\nabla}u).\vec{k}\right) \tag{A.22}$$

Neglecting the thermal conductivity variation term and placing equation (A.21) and (A.22) into equation (A.18) one gets;

$$\frac{\partial h}{\partial t} = -\vec{\nabla}.(\vec{V}h) + \frac{\gamma k}{Re.Pr}\nabla^2 h + \Theta(\omega,\rho,\beta,h) \tag{A.23}$$

where

$$\Theta = \Theta_1 + \Theta_2$$

$$\Theta_1 = (2-\gamma)\beta h$$

$$\Theta_2 = \frac{\gamma\mu}{\rho Re}\left\{\frac{4}{3}\beta^2 + \omega^2 + 4(\vec{\nabla}v \times \vec{\nabla}u).\vec{k}\right\}$$

(4) <u>The Density Equation</u>

The continuity equation (2.2) can be written as follows.

$$\frac{1}{\rho}\frac{\partial\rho}{\partial t} + \vec{\nabla}.\vec{V} + \frac{\vec{V}}{\rho}\,.\,\vec{\nabla}\rho = 0 \tag{A.24}$$

Further, noting that

$$\beta = \vec{\nabla}.\vec{V}$$

thus equation (A.24) becomes,

$$\frac{\partial \ln\rho}{\partial t} = -\beta - \vec{V}.\vec{\nabla}\ln\rho \qquad (A.25)$$

In conservative form, equation (A.25) can be written as follows

$$\frac{\partial \ln\rho}{\partial t} = -\vec{\nabla}.(\vec{V}\ln\rho) + \Gamma \qquad (A.26)$$

where

$$\Gamma = \beta(\ln\rho - 1)$$

APPENDIX B

TRANSFORMATION RELATIONS

The transformation relations used in the derivation of the kinetic transport equations are given here. The following expressions relate the mathematical operations done in the physical plane, ph, with those that performed in the transformed plane, T.

$$(\vec{\nabla} f . \vec{\nabla} g)_{ph.} = \frac{1}{H^2} (\vec{\nabla} f . \vec{\nabla} g)_T \tag{B.1}$$

$$(\nabla f x \nabla g)_{ph.} = \frac{1}{H^2} (\vec{\nabla} f \; x \; \vec{\nabla} g)_T \tag{B.2}$$

$$(\nabla^2 f)_{ph.} = \frac{1}{H^2} (\nabla^2 f)_T \tag{B.3}$$

$$(\vec{\nabla} . \; (f\vec{V}))_{ph.} = \frac{1}{H^2} (\vec{\nabla} . \; (f\vec{V}))_T \tag{B.4}$$

where,

(i) H is the transformation scale factor

(ii) f and g are scalar functions which are invariant with the transformation.

(iii) $\vec{V}_{ph}$ is the velocity vector in the physical plane, while $\vec{V}_T$ is the apparent velocity vector in the transformed plane and its components (V_θ, V_r) are given by equations (2-27) and (2-28).

The components of the velocity vector V in the physical plane (u,v) are related to the velocity components (V_θ, V_r) as follows:

$$u = \frac{1}{H^2}\left(-V_\theta \frac{dy}{dr} + \frac{1}{r} V_r \frac{dy}{d\theta}\right) \tag{B.5}$$

$$v = \frac{1}{H^2}\left(V_r \frac{dy}{dr} + \frac{1}{r} V_\theta \frac{dy}{d\theta}\right) . \tag{B.6}$$

where y and x are the Cartesian coordinates in the physical plane. The transformed quantities can be expanded in polar coordinates (s-θ) as follows:

$$(\vec{\nabla}f \cdot \vec{\nabla}g)_T = \left[\left(\frac{1}{r-c}\right)^2 \frac{\partial f}{\partial s} \cdot \frac{\partial g}{\partial s} + \frac{1}{r^2} \frac{\partial f}{\partial \theta} \cdot \frac{\partial g}{\partial \theta}\right] \tag{B.7}$$

$$(\vec{\nabla}f \times \vec{\nabla}g)_T = \frac{1}{r(r-c)}\left(\frac{\partial f}{\partial s} \cdot \frac{\partial g}{\partial s} - \frac{\partial f}{\partial \theta} \cdot \frac{\partial g}{\partial \theta}\right) \tag{B.8}$$

$$(\nabla^2 f)_T = \left(\frac{1}{r-c}\right)^2 \frac{\partial^2 f}{\partial s^2} + \left(\frac{1}{r(r-c)} - \left(\frac{1}{r-c}\right)^2 \frac{\partial f}{\partial s} + \frac{1}{r} \frac{\partial^2 f}{\partial \theta^2}\right. \tag{B.9}$$

where s is the stretched radial coordinate in the transformed polar plane and is given by;

$$r = e^s + c \tag{B.10}$$

APPENDIX C

EVALUATION OF INTEGRALS IN EQUATIONS (4.3) - (4.5)

The integrals that need to be evaluated are

$$I_m = r_o \int_o^{2\pi} \frac{\cos m\theta_o \left[r_o \cos(\theta_o - \theta) - r \right]}{r_o^2 + r^2 - 2r_o r \cos(\theta_o - \theta)} \, d\theta_o \tag{C.1}$$

$$J_m = r_o \int_o^{2\pi} \frac{\sin m\theta_o \left[r_o \cos(\theta_o - \theta) - r \right]}{r_o^2 + r^2 - 2r_o r \cos(\theta_o - \theta)} \, d\theta_o \tag{C.2}$$

$$\tilde{I}_m = r_o^2 \int_o^{2\pi} \frac{\cos m\theta_o \sin(\theta_o - \theta)}{r_o^2 + r^2 - 2r_o r \cos(\theta_o - \theta)} \, d\theta_o \tag{C.3}$$

$$\tilde{J}_m = r_o^2 \int_o^{2\pi} \frac{\sin m\theta_o \sin(\theta_o - \theta)}{r_o^2 + r^2 - 2r_o r \cos(\theta_o - \theta)} \, d_o \tag{C.4}$$

where $0 \leq m \leq N$. If the following complex variables are defined as

$$W_m = I_m + i J_m \tag{C.5}$$

$$\tilde{W}_m = I_m + i J_m \tag{C.6}$$

and

$$z_o = e^{i\theta_o} = \cos\theta_o + i \sin\theta_o \tag{C.7}$$

$$z = e^{i\theta} = \cos\theta + i \sin\theta \tag{C.8}$$

where $i = \sqrt{-1}$. The quantities W_m and $\tilde{W}_m$ could be reexpressed as follows after the variable transformation from θ, θ_o to z, z_o :

$$W_m = -\frac{1}{2ir}\int \frac{z_o^{m-1}\left[r_o(z_o^2 + z^2) - 2rzz_o\right]}{(z_o - \frac{r}{r_o}z)(z_o - \frac{r_o}{r}z)}\, dz_o \qquad (C.9)$$

$$\tilde{W}_m = \frac{r_o}{2r}\oint \frac{z_o^{m-1}(z_o^2 - z^2)}{(z_o - \frac{r}{r_o}z)(z_o - \frac{r_o}{r}z)}\, dz_o \qquad (C.10)$$

By using of residue theorem, the integrals in equations (C.9) and (C.10) are evaluated explicitly and the results are

(1) for $r < r_o$:

$$W_o = 0 \qquad (C.11)$$

$$W_m = \pi(\frac{r}{r_o})^{m-1} z^m \qquad (C.12)$$

$$\tilde{W}_o = 0 \qquad (C.13)$$

$$\tilde{W}_m = i\pi(\frac{r}{r_o})^{m-1} z^m \qquad (C.14)$$

(2) for $r > r_o$:

$$W_o = -2\pi(\frac{r_o}{r}) \qquad (C.15)$$

$$W_m = -\pi(\frac{r_o}{r})^{m+1} z^m \qquad (C.16)$$

$$\tilde{W}_o = 0 \qquad (C.17)$$

$$\tilde{W}_m = i\pi(\frac{r_o}{r})^{m+1} z^m \qquad (C.18)$$

where $1 \leq m \leq N$. The values of I_m, J_m, I_m, J_m's could be determined easily by equations (C.5) and (C.6). Thus

(1) for $r \leq r_o$:

$$I_o = 0 \tag{C.19}$$

$$I_m = \pi(\frac{r}{r_o})^{m-1} \cos m\theta \tag{C.20}$$

$$J_o = 0 \tag{C.21}$$

$$J_m = \pi(\frac{r}{r_o})^{m-1} \sin m\theta \tag{C.22}$$

$$I_o = 0 \tag{C.23}$$

$$I_m = -\pi(\frac{r}{r_o})^{m-1} \sin m\theta \tag{C.24}$$

$$\tilde{J}_o = 0 \tag{C.25}$$

$$\tilde{J}_m = \pi(\frac{r}{r_o})^{m-1} \cos m\theta \tag{C.26}$$

(2) for $r > r_o$:

$$I_o = -2\pi(\frac{r_o}{r}) \tag{C.27}$$

$$I_m = -\pi(\frac{r_o}{r})^{m+1} \text{ccs } m\theta \tag{C.28}$$

$$J_o = 0 \tag{C.29}$$

$$J_m = -\pi(\frac{r_o}{r})^{m+1} \sin m \tag{C.30}$$

$$I_o = 0 \tag{C.31}$$

$$I_m = -\pi(\frac{r_o}{r})^{m+1} \sin m\theta \tag{C.32}$$

$$J_o = 0 \tag{C.33}$$

$$J_m = \pi(\frac{r_o}{r})^{m+1} \cos m\theta \tag{C.34}$$

The integrals that need to be evaluated in kinetics are

$$I_m = r_o \int_o^{2\pi} \frac{\cos m\theta_o \left[r_o - r\cos(\theta_o - \theta)\right]}{r_o^2 + r^2 - 2r_o r\cos(\theta_o - \theta)} d\theta_o \tag{C.35}$$

$$J_m = r_o \int_o^{2\pi} \frac{\sin m\theta_o \left[r_o - r\cos(\theta_o - \theta)\right]}{r_o^2 + r^2 - 2r_o r\cos(\theta_o - \theta)} d\theta_o \tag{C.36}$$

$$\tilde{I}_m = r_o r \int_o^{2\pi} \frac{\cos m\theta_o \sin(\theta_o - \theta)}{r_o^2 + r^2 - 2r_o r\cos(\theta_o - \theta)} d\theta_o \tag{C.37}$$

$$\tilde{J}_m = r_o r \int_o^{2\pi} \frac{\sin m\theta_o \sin(\theta_o - \theta)}{r_o^2 + r^2 - 2r_o r\cos(\theta_o - \theta)} d\theta_o \tag{C.38}$$

also the complex quantities are

$$W_m = I_m + i\, J_m \tag{C.39}$$

$$\tilde{W}_m = \tilde{I}_m + i\, \tilde{J}_m \tag{C.40}$$

Following the same procedure as in kinematics, the following expressions are obtained

$$W_m = \frac{1}{2ir} \oint \frac{z_o^{m-1}\left[r(z_o^2 + z^2) - 2r_o z_o z\right]}{(z_o - \frac{r}{r_o} z)(z_o - \frac{r_o}{r} z)} d_{z_o} \tag{C.41}$$

$$\tilde{W}_m = \frac{1}{2}\oint \frac{z_o^{m-1}\,(z_o^2 - z^2)}{(z_o - \frac{r}{r_o}z)(z_o - \frac{r_o}{r}z)}\,dz_o \tag{C.42}$$

and the final results are

(1) for $r < r_o$:

$$I_o = 2\pi \tag{C.43}$$

$$I_m = \pi(\frac{r}{r_o})^m \cos m\theta \tag{C.44}$$

$$J_o = 0 \tag{C.45}$$

$$J_m = \pi(\frac{r}{r_o})^m \sin m \tag{C.46}$$

$$\tilde{I}_o = 0 \tag{C.47}$$

$$\tilde{I}_m = -\pi(\frac{r}{r_o})^m \sin m\theta \tag{C.48}$$

$$\tilde{J}_o = 0 \tag{C.49}$$

$$\tilde{J}_m = \pi(\frac{r}{r_o})^m \sin m\theta \tag{C.50}$$

(2) for $r > r_o$:

$$I_o = 0 \tag{C.51}$$

$$I_m = -\pi(\frac{r_o}{r})^m \cos m\theta \tag{C.52}$$

$$J_o = 0 \tag{C.53}$$

$$J_m = -\pi(\frac{r_o}{r})^m \sin m\theta \tag{C.54}$$

$$\tilde{I}_o = 0 \tag{C.55}$$

$$\tilde{I}_m = -\pi(\frac{r_o}{r})^m \sin m\theta \tag{C.56}$$

$$\tilde{J}_o = 0 \tag{C.57}$$

$$\tilde{J}_m = \pi(\frac{r_o}{r})^m \cos m\theta \tag{C.58}$$

where $1 \leq m \leq N$.

APPENDIX D

DERIVATION OF RELATIONSHIPS BETWEEN FOURIER COEFFICIENTS

The following expression for v_r is obtained after substituting equations (4.6, 4.8) into equation (4.3)

$$v_r = \frac{1}{2\pi}\int_o^1 \left[\alpha_o \tilde{I}_o + \sum_{n=1}^{N} (\alpha_n \tilde{I}_n + \beta_n \tilde{J}_n)\right] dr_o$$

$$+ \frac{1}{2\pi\rho}\left[s_o(1)\, I_o + \sum_{n=1}^{N} (s_n(1)\, I_n + t_n(1)\, J_n)\right]$$

$$- \frac{1}{2\pi}\left[p_o(1)\, \tilde{I}_o + \sum_{n=1}^{N} (p_n(1)\, \tilde{I}_n + q_n(1)\, \tilde{J}_n)\right] \quad \text{(D.1)}$$

where I, $\tilde{I}$, J, $\tilde{J}$ are those quantities defined in Section (i), Appendix E. From equations (C.11) - (C.34)

$$v_r = -\frac{1}{2}\int_o^r \sum_{n=1}^{N}\left[\alpha_n \left(\frac{r_o}{r}\right)^{n+1} \sin n\theta - \beta_n \left(\frac{r_o}{r}\right)^{n+1} \cos n\theta\right] dr_o$$

$$-\frac{1}{2}\int_r^1 \sum_{n=1}^{N}\left[\alpha_n \left(\frac{r}{r_o}\right)^{n-1} \sin n\theta - \beta_n \left(\frac{r}{r_o}\right)^{n-1} \cos n\theta\right] dr_o$$

$$+\frac{1}{2}\sum_{n=1}^{N}\left[s_n(1)\, r^{n-1} \cos n\theta + t_n(1)\, r^{n-1} \sin n\theta\right]$$

$$+\frac{1}{2}\sum_{n=1}^{N}\left[p_n(1)\, r^{n-1} \sin n\theta - q_n(1)\, r^{n-1} \cos n\theta\right] \quad \text{(D.2)}$$

If v_r is also expanded in Fourier series (as in equation 4.6)), the corresponding Fourier coefficients are related by

$$s_o = 0 \tag{15}$$

$$s_n = \frac{1}{2} \int_o^r \beta_n (\frac{r_o}{r})^{n+1} dr_o + \int_r^1 \beta_n (\frac{r}{r_o})^{n-1} dr_o$$

$$+ \frac{1}{2} s_n(1)\, r^{n-1} - \frac{1}{2} q_n(1)\, r^{n-1} \tag{16}$$

$$t_n = -\frac{1}{2} \int_o^r \alpha_n (\frac{r_o}{r})^{n+1} dr_o - \frac{1}{2} \int_r^1 \alpha_n (\frac{r}{r_o})^{n-1} dr_o$$

$$+ \frac{1}{2} t_n(1)\, r^{n-1} + \frac{1}{2} p_n(1)\, r^{n-1} \tag{17}$$

where $1 \leq n \leq N$. Similarly, the expression for v_θ from equation (4.4)

$$v_\theta = \frac{1}{2} \int_o^1 \left[\alpha_o\, I_o + \sum_{n=1}^{N} (\alpha_n I_n + \beta_n\, J_n)\right] dr_o$$

$$+ \frac{1}{2\pi}\left[s_o(1)\, \tilde{I}_o + \sum_{n=1}^{N} (s_n(1)\, \tilde{I}_n + t_n(1)\, \tilde{J}_n)\right]$$

$$+ \frac{1}{2\pi}\left[p_o(1)\, I_o + \sum_{n=1}^{N} (p_n(1)\, I_n + q_n(1)\, J_n)\right] \tag{D.3}$$

which is

$$v_\theta = \frac{1}{2} \int_o^r \sum_{n=1}^{N} \left[\alpha_n (\frac{r_o}{r})^{n+1} \cos n\theta + \beta_n (\frac{r_o}{r})^{n+1} \sin n\theta\right] dr_o$$

$$- \frac{1}{2} \int_r^1 \sum_{n=1}^{N} \left[\alpha_n (\frac{r}{r_o})^{n-1} \cos n\theta + \beta_n (\frac{r}{r_o})^{n-1} \sin n\theta\right] dr_o$$

$$- \frac{1}{2} \sum_{n=1}^{N} \left[s_n(1)\, r^{n-1} \sin n\theta - t_n(1)\, r^{n-1} \cos n\theta\right]$$

$$+ \frac{1}{2} \sum_{n=1}^{N} \left[p_n(1)\, r^{n-1} \cos n\theta + q_n(1)\, r^{n-1} \sin n\theta\right] \tag{D.4}$$

Expanding v_θ in Fourier series as in equation (4.7) the corresponding coefficients are related by equations (4.12)-(4.14).

By expanding ωv_r, ωv_θ in equations (4.18) and (4.19) equation (4.5) could be expressed as

$$
\begin{aligned}
\omega = & - \frac{Re}{2\pi} \int_o^1 \Big[\xi_o I_o + \sum_{n=1}^{N} (\xi_n I_n + \eta_n J_n)\Big] dr_o \\
& - \frac{Re}{2\pi} \int_o^1 \Big[\mu_o I_o + \sum_{n=1}^{N} \mu_n I_n + \zeta_n J_n)\Big] dr_o \\
& + \frac{Re}{2\pi} \Big[f_o(1)\, I_o + \sum_{n=1}^{N} (f_n(1) I_n + g_n(1) J_n)\Big] \\
& + \frac{1}{2\pi} \Big[\alpha_o(1) I_o + \sum_{n=1}^{N} (\alpha_n(1) I_n + \beta_n(1) J_n)\Big]
\end{aligned} \tag{D.5}
$$

where I, I, J, J's are those quantities defined in Section (ii) Appendix C, and f_o, f_n, g_n's are the Fourier coefficients of the total pressure.

$$
h = f_o + \sum_{n=1}^{N} (f_n \cos n\theta + g_n \sin n\theta) \tag{D.6}
$$

By the results of equations (C.43)-(C.58), equation (D.5) becomes

$$
\begin{aligned}
\omega = & \frac{Re}{2} \int_o^r \sum_{n=1}^{N} \left(\frac{r_o}{r}\right)^n \Big[(\xi_n - \zeta_n) \cos n\theta + (\eta_n + \mu_n) \sin n\theta\Big] dr_o \\
& - \frac{Re}{2} \int_r^1 \Big\{ 2\xi_o + \sum_{n=1}^{N} \left(\frac{r}{r_o}\right)^n \Big[(\xi_n + \zeta_n) \cos n\theta \\
& + (\eta_n - \mu_n) \sin n\theta\Big]\Big\} dr_o \\
& + \frac{Re}{2} \sum_{n=1}^{N} \Big[- f_n(1)\, r^n \sin n\theta + g_n(1)\, r^n \cos n\theta\Big]
\end{aligned}
$$

C-2

$$+ \qquad + \sum_{n=1}^{N} \alpha_n(1)\, r^n \cos n\theta + \beta_n(1)\, r^n \sin n\theta \qquad (D.7)$$

Thus, in using the Fourier series expansion for ω (equation 4.8), the corresponding coefficients are related by

$$\alpha_o = \alpha_o(1) - Re \int_r^1 \xi_o \, dr_o \qquad (21)$$

$$\alpha_n = \frac{Re}{2} \int_o^r (\xi_n - \zeta_n)(\frac{r_o}{r})^n \, dr_o - \frac{Re}{2} \int_r^1 (\xi_n + \zeta_n)(\frac{r}{r_o})^n \, dr_o$$

$$+ \frac{Re}{2} g_n(1)\, r^n + \frac{1}{2} \alpha_n(1)\, r^n \qquad (D.8)$$

$$\beta_n = \frac{Re}{2} \int_o^r (\eta_n + \mu)(\frac{r_o}{r})^n \, dr_o + \frac{Re}{2} \int_r^1 (\mu_n - \eta_n)(\frac{r}{r_o})^n \, dr_o$$

$$- \frac{Re}{2} f_n(1)\, r^n + \frac{1}{2} \beta_n(1)\, r^n \qquad (D.9)$$

where $1 \leq n \leq N$. Equations (D.8) and (D.9) are equivalent to equations (4.16) and (4.17) respectively, where the terms $g_n(1)$ and $f_n(1)$ are cancelled by applying the equations (D.8) and (D.9) on the boundary.

APPENDIX E

THE INTEGRAL REPRESENTATIONS FOR A DOUBLY-CONNECTED REGION

The boundary integrals in equations (4.3) and (4.4) consist of two parts, B_1 and B_2

$$\oint_B = \oint_{B_1} - \oint_{B_2} \tag{E.1}$$

At the interior boundary B_2, the velocity components are assumed to be known. The Fourier coefficients of the velocities at B_2 are zero except $p_o(R)$, which is the magnitude of the circumferential velocity at r=R due to the solid rotation.

The equations (D.1) for the velocity v_r needs to be rewritten to include the B_2 effect:

$$\begin{aligned} v_r = {} & \frac{1}{2\pi} \int_R^1 \left[\alpha_o I_o + \sum_{n=1}^{N} (\alpha_n \tilde{I}_n + \beta_n \tilde{J}_n)\right] dr_o \\ & + \frac{1}{2\pi} \left[s_o(1)\, I_o + \sum_{n=1}^{N} (s_n(1)\, I_n + t_n(1)\, J_n)\right] \\ & - \frac{1}{2\pi} \left[s_o(R)\, I_o + \sum_{n=1}^{N} (s_n(R)\, I_n + t_n(R)\, J_n)\right] \\ & - \frac{1}{2\pi} \left[p_o(1)\, \tilde{I}_o + \sum_{n=1}^{N} (p_n(1)\, \tilde{I}_n + q_n(1)\, \tilde{J}_n)\right] \\ & + \frac{1}{2\pi} \left[p_o(R)\, \tilde{I}_o + \sum_{n=1}^{N} (p_n(R)\, \tilde{I}_n + q_n(R)\, \tilde{J}_n)\right] \end{aligned} \tag{E.2}$$

where $s_o(R)$, $p_o(R)$, $s_n(R)$, $t_n(R)$, $p_n(R)$, $q_n(R)$ are the Fourier coefficients of the velocities at r=R. Thus

$$s_o = 0 \tag{15}$$

$$s_n = \frac{1}{2}\int_R^r \beta_n\left(\frac{r_o}{r}\right)^{n+1} dr_o + \int_r^1 \beta_n\left(\frac{r}{r_o}\right)^{n-1} dr_o$$

$$+ \frac{1}{2}\, s_n(1)\, r^{n-1} - \frac{1}{2} q_n(1)\, r^{n-1} \tag{E.3}$$

$$t_n = -\frac{1}{2}\int_R^r \alpha_n\left(\frac{r_o}{r}\right)^{n+1} dr_o - \frac{1}{2}\int_r^1 \alpha_n\left(\frac{r}{r_o}\right)^{n-1} dr_o$$

$$+ \frac{1}{2}\, t_n(1)\, r^{n-1} + \frac{1}{2}\, p_n(1)\, r^{n-1} \tag{E.4}$$

where $1 \leq n \leq N$. Similarly, the velocity v_θ is reexpressed as:

$$v_\theta = \frac{1}{2\pi}\int_R^1 \left[\alpha_o I_o + \sum_{n=1}^{N} (\alpha_n I_n + \beta_n J_n)\right] dr_o$$

$$+ \frac{1}{2\pi}\left[s_o(1)\, \tilde{I}_o + \sum_{n=1}^{N} (s_n(1)\, \tilde{I}_n + t_n(1)\, \tilde{J}_n)\right]$$

$$- \frac{1}{2\pi}\left[s_o(R)\, I_o + \sum_{n=1}^{N} (s_n(R)\, I_n + t_n(R)\, J_n)\right]$$

$$+ \frac{1}{2\pi}\left[p_o(1)\, \tilde{I}_o + \sum_{n=1}^{N} (p_n(1)\, \tilde{I}_n + q_n(1)\, \tilde{J}_n)\right]$$

$$- \frac{1}{2\pi}\left[p_o(R)\, \tilde{I}_o + \sum_{n=1}^{N} (p_n(R)\, \tilde{I}_n + q_n(R)\, \tilde{J}_n)\right] \tag{E.5}$$

By using equations (4.7) and (C.17) the following relations are obtained

$$p_o = \int_R^r \alpha_o(\frac{r_o}{r})\, dr_o + \frac{R}{r}\, p_o(R) \tag{E.6}$$

$$p_n = \frac{1}{2}\int_R^r \alpha_n\,(\frac{r_o}{r})^{n+1}\, dr_o - \frac{1}{2}\int_r^1 \alpha_n(\frac{r}{r_o})^{n-1}\, dr_o$$

$$+ \frac{1}{2}\, t_n(1)\, r^{n-1} + \frac{1}{2}\, p_n(1)\, r^{n-1} \tag{E.7}$$

$$q_n = \frac{1}{2}\int_R^r \beta_n(\frac{r_o}{r})^{n+1}\, dr_o - \frac{1}{2}\int_r^1 \beta_n(\frac{r}{r_o})^{n-1}\, dr_o$$

$$- \frac{1}{2}\, s_n(1)\, r^{n-1} + \frac{1}{2}\, q_n(1)\, r^{n-1} \tag{E.8}$$

where $1 \leq n \leq N$.

The equation (D.5) becomes

$$\omega = -\frac{Re}{2\pi}\int_R^1 [\xi_o I_o + \sum_{n=1}^{N}(\xi_n I_n + \eta_n J_n)]\, dr_o$$

$$- \frac{Re}{2}\int_R^1 [\mu_o \tilde{I}_o + \sum_{n=1}^{N}(\mu_n \tilde{I}_n + \zeta_n \tilde{J}_n)]\, dr_o$$

$$+ \frac{Re}{2\pi}\,[f_o(1)\,\tilde{I}_o + \sum_{n=1}^{N}(f_n(1)\,\tilde{I}_n + g_n(1)\,\tilde{J}_n)]$$

$$- \frac{Re}{2\pi}\,[f_o(R)\,\tilde{I}_o + \sum_{n=1}^{N}(f_n(R)\,\tilde{I}_n + g_n(R)\,\tilde{J}_n)]$$

$$+ \frac{1}{2\pi}\,[\alpha_o(1)\, I_o + \sum_{n=1}^{N}(\alpha_n(1)\, I_n + \beta_n(1)\, J_n)]$$

$$- \frac{1}{2\pi}\,[\alpha_o(R)\, I_o + \sum_{n=1}^{N}(\alpha_n(R)\, I_n + \beta_n(R)\, J_n)] \tag{E.9}$$

where $f_o(R)$, $f_n(R)$ and $g_n(R)$ are the Fourier coefficients of the total pressure at r=R. By using the equations (C.43)-(C.58):

$$\omega = \frac{Re}{2} \int_R^r \sum_{n=1}^{N} \left(\frac{r_o}{r}\right)^n \left[(\xi_n - \zeta_n)\cos n\theta + (\eta_n + \mu_n)\sin n\theta\right] dr_o$$

$$- \frac{Re}{2} \int_r^1 \left\{ 2\xi_o + \sum_{n=1}^{N} \left(\frac{r}{r_o}\right)^n \left[(\xi_n + \zeta_n)\cos n\theta + (\eta_n - \mu_n)\sin n\theta\right] dr_o \right.$$

$$+ \frac{Re}{2} \sum_{n=1}^{N} \left[- f_n(1) r^n \sin n\theta + g_n(1)\, r^n \cos n\theta\right]$$

$$- \frac{Re}{2} \sum_{n=1}^{N} \left[- f_n(R)\left(\frac{R}{r}\right)^n \sin n\theta + g_n(R)\left(\frac{R}{r}\right)^n \cos n\theta\right] \tag{E.10}$$

REFERENCES

1. J.C. Wu, "Integral Representation of Field Variables for the Finite Element Solution of Viscous Flow Problems," Proceedings of the 1974 Conference on Finite Element Methods in Engineering, pp. 27-840, Clarendon Press, 1974.

2. Sankar, N.L. and Tassa, Y., "Reynolds Number and Compressibility Effects on Dynamic Stall of a NACA 0012 Airfoil," AIAA Paper 80-0010.

3. Sampath, S., "A Numerical Study of Incompressible Viscous Flow around Airfoils," Ph.D. Thesis, Georgia Institute of Technology, Atlanta, Georgia, September, 1977.

4. Sankar, N.L., "Numerical Study of Unsteady Flow over Airfoils," Ph.D. Thesis, Georgia Institute of Technology, Atlanta, Georgia November 1977.

5. Rizk, Y., "An Integral-Representation Approach for Time Dependent Viscous Flows," Ph.D. Thesis, Georgia Institute of Technology, Atlanta, Georgia, 1980.

6. Gulcat, U., "Separate Numerical Treatment of Attached and Detached Flow Regions in General Viscous Flows," Ph.D. Thesis, Georgia Institute of Technology, Atlanta, Georgia, 1981.

7. Mehta, U.B., "Starting Vortex, Separation Bubbles and Stall -A Numerical Study of Laminar Unsteady Flow around an Airfoil," Ph.D. Thesis, Illinois Inst. of Technology, Chicago, Illinois, 1972.

8. Ames, W.F., Numerical Methods for Partial Differential Equations, Academic Press, pp. 73-82, 1977.

9. Desideri, J.A., Steger, J.L., and Tannehill, J.C., "On Improving The Iterative Convergence Properties of an Implicit Approximate Factorization Finite Difference Algorithm," NASA TM 73495, June, 1978.

10. Ballhaus, W.F., Jameson, A. and Albert, J., "Implicit Approximate Factorization Scheme for Steady Transonic Flow Problems," AIAA Journal, Vol. 16, No. 6, June, 1978.

11. ElRefaee M.M., "A Numerical Study of Laminar Unsteady Compressible Flows over Airfoils," Ph.D. Thesis, Georgia Institute of Technology, Atlanta, Georgia, May 1981.

12. Burggraf, O.R., "Analytical and Numerical Studies of the Structure of Steady Separated Flows," J. Fluid Mechanics, Vol. 24, pp. 113-151, 1966.

13. Batchelor, G.K., "On Steady Laminar Flow with Closed Streamlines at Large Reynolds Number," J. Fluid Mechanics, Vol. 1, pp. 177-190, 1956.

14. Kuwahara, K., Imai I., "Steady Viscous Flow within a Circular Boundary," The Physics of Fluids, Supplement II, pp. 94-101, 1969.

15. Wood, W.W., "Boundary Layers Whose Streamlines are Closed," J. Fluid Mechanics, Vol. 2, pp. 77-87, 1957.

16. Gottlieb, D. and Orszag S.A., Numerical Analysis of Spectral Methods: Theory and Applications, SIAM Publications, 1977.